Aggregation of HAPLN2, a component of the perinodal extracellular matrix, is a hallmark of physiological brain aging in mice

Ayaka Watanabe[1¶], Shoshiro Hirayama[1¶], Itsuki Kominato[1], Sybille Marchese[2], Pietro Esposito[2], Vanya Metodieva[2], Hiroshi Kameda[3], Terunori Sano[4], Sho Takatori[5], Masaki Takao[4], Masato Koike[3], Juan Alberto Varela[6], Taisuke Tomita[5], Shigeo Murata[1*]

[1] Laboratory of Protein Metabolism, Graduate School of Pharmaceutical Sciences, the University of Tokyo, Tokyo, Japan

[2] School of Biology, University of St Andrews, St Andrews, United Kingdom

[3] Department of Cell Biology and Neuroscience, Juntendo University Graduate School of Medicine, Tokyo, Japan

[4] Department of Clinical Laboratory, National Centre of Neurology and Psychiatry, Tokyo, Japan

[5] Laboratory of Neuropathology and Neuroscience, Graduate School of Pharmaceutical Sciences, the University of Tokyo, Tokyo, Japan

[6] School of Physics and Astronomy, University of St Andrews, St Andrews, United Kingdom

[*] Corresponding author

Email: smurata@g.ecc.u-tokyo.ac.jp (SMurata)

¶These authors contributed equally to this work.

Abstract

Protein aggregation is a hallmark of neurodegenerative diseases and is also observed in the brains of elderly individuals without such conditions, suggesting that aging drives the accumulation of protein aggregates. However, the comprehensive understanding of age-dependent protein aggregates involved in brain aging remains unclear. Here, we investigated proteins that become sarkosyl-insoluble with age and identified hyaluronan and proteoglycan link protein 2 (HAPLN2), a hyaluronic acid-binding protein of the extracellular matrix at the nodes of Ranvier, as an age-dependent aggregating protein in mouse brains. Elevated hyaluronic acid levels and impaired microglial function reduced the clearance of HAPLN2, leading to its accumulation. HAPLN2 oligomers induced microglial inflammatory responses both *in vitro* and *in vivo*. Furthermore, age-associated HAPLN2 aggregation was also observed in the human cerebellum. These findings suggest that HAPLN2 aggregation results from age-related decline in brain homeostasis and may exacerbate the brain environment by activating microglia. This study provides new insights into the mechanisms underlying cerebellar aging and highlights the role of HAPLN2 in age-associated changes in the brain.

Author Summary

To identify age-dependent protein aggregates unrelated to disease, we analyzed the sarkosyl-insoluble proteome of young and aged mouse brains. We discovered that hyaluronan and proteoglycan link protein 2 (HAPLN2), a hyaluronic acid-binding protein existing in the nodal extracellular matrix, accumulated with age. Age-dependently accumulated HAPLN2 formed large protein aggregates that cannot be solubilized by the anionic detergent sarkosyl or by hyaluronidase digestion. In addition, HAPLN2 formed irregularly shaped puncta that were mislocalized from the nodes of Ranvier in the cerebellar white matter of not only aged mice but also aged human brains. Oligomers of full-length HAPLN2 specifically induced microglial activation *in vitro* and *in vivo*. Our findings suggest that the accumulation of HAPLN2 aggregates is a new hallmark of brain aging and a possible factor contributing to brain inflammation.

Introduction

Protein aggregation is associated with a wide range of physiological declines, including neurodegenerative diseases, with amyloid β (Aβ) and tau being prominent examples. These proteins aggregate to cause neurodegenerative diseases such as Alzheimer's disease, disrupting neuronal function and ultimately causing cell death. Intracellular aggregates interfere with essential cellular processes such as protein folding, trafficking, and degradation, resulting in the accumulation of misfolded proteins and cellular stress [1]. This disruption impairs crucial neuronal functions, including transcription [2], mitochondrial function [3], and stress granule dynamics [4, 5]. In neurodegenerative diseases, the accumulation of protein aggregates is also observed in the extracellular space. These aggregates activate microglia, triggering the release of pro-inflammatory cytokines and neurotoxic factors, leading to chronic inflammation detrimental to neuronal health [6].

The impairment of clearance systems in both intracellular and extracellular spaces is thought to be responsible for the accumulation of aberrant protein aggregates. The main intracellular pathways for clearing abnormal proteins are the ubiquitin-proteasome system [7] and the autophagy-lysosome system [8, 9]. Additionally, extracellular mechanisms such as phagocytosis and secretion of proteases by microglia [10, 11], and the glymphatic system contribute to the clearance of protein aggregates from the brain [12]. However, aging is associated with a decline in the capacity of these mechanisms to maintain proteostasis, making organisms more susceptible to protein aggregation. This decline is attributed to factors such as reduced efficiency of protein degradation pathways, decreased expression of chaperone proteins, impaired cellular stress responses, and microglial senescence [13, 14].

Interestingly, aggregates of wild-type Aβ, tau, and TMEM106B have been observed in the brains of non-demented elderly individuals [15–17]. This suggests that protein aggregation is not merely a consequence of neurodegenerative diseases but also an inherent aspect of the aging process itself, raising the possibility that age-dependent protein aggregates contribute to the broader physiological decline during aging.

87 Indeed, the detrimental effects of age-related protein aggregation have been demonstrated
88 in model organisms. In *Caenorhabditis elegans*, the accumulation of both intracellular
89 and extracellular protein aggregates is associated with reduced lifespan, regardless of
90 disease state. In contrast, removing these aggregates extend lifespan. For example,
91 reduced daf-2 function suppresses protein aggregation and extends lifespan, whereas
92 deficiency in daf-16 or hsf-1 induces protein aggregation and shortens lifespan [18–22].
93 Furthermore, analysis of RIPA buffer-insoluble and sodium deoxycholate-insoluble
94 proteins by mass spectrometry has revealed that protein aggregation occurs extensively
95 during physiological aging in the absence of disease [22, 23]. These findings suggest that
96 the clearance of age-related protein aggregates in *C. elegans* is crucial for maintaining
97 individual health.

98 An extracellular protein quality control mechanism exists that disposes of extracellular
99 waste in *C. elegans*. Coelomocytes remove extracellular debris through non-specific
100 phagocytosis [24]. Moreover, overexpression of extracellular chaperones in the
101 pseudocoelom suppresses the accumulation of aggregates and extends lifespan [25].
102 These findings highlight the importance of extracellular protein quality control and
103 emphasize the essential role to maintain proteostasis in the extracellular space to ensure
104 healthy aging.

105 In contrast to these studies about *C. elegans*, less is known about how age-dependent
106 protein aggregates contribute to the aging process in mammals. To address this gap, we
107 employed proteomic analyses to identify proteins that aggregate and accumulate in the
108 mouse brain with age. Our investigation identified hyaluronan and proteoglycan link
109 protein 2 (HAPLN2), a perinodal extracellular matrix constituent protein, as an age-
110 dependent protein aggregate. We found that HAPLN2 accumulates in the cerebellar white
111 matter and is mislocalized from its typical location at the nodes of Ranvier in aged mouse
112 brains. Further investigation using recombinant protein revealed that HAPLN2 forms
113 aggregates under acidic conditions and in the presence of hyaluronic acid, mimicking
114 age-related changes in the brain microenvironment. Importantly, we also observed age-
115 dependent HAPLN2 aggregation in human brain sections. These findings suggest that
116 HAPLN2 aggregation may be a conserved hallmark of brain aging across mammalian

species. Our study highlights the importance of investigating age-related protein aggregation beyond the context of specific neurodegenerative diseases and suggests a potential role for HAPLN2 aggregates in brain aging, possibly by inducing microglial activation and neuroinflammation.

Results

Proteomic analyses of aged mouse brains identified proteins that accumulate in the sarkosyl-insoluble fraction with age

To identify proteins that aggregate in an age-dependent manner, we enriched detergent-insoluble proteins from the whole brains of young (2-month-old) and aged (24-month-old) mice using 1% N-lauryl-sarcosine (sarkosyl) fractionation (Fig 1A). Sarkosyl is a well-established detergent that solubilizes natively folded proteins while enriching protein aggregates associated with neurodegenerative diseases in its insoluble P2 fraction (Fig 1A) [26–31]. Proteins in the sarkosyl-insoluble P2 fraction were subjected to label-free quantitative proteomics. We identified 31 proteins that increased more than 5-fold in the brains of aged mice compared to young mice as candidates for age-dependent protein aggregates (S1 Table).

Age-related accumulation of proteins associated with neurodegenerative diseases is attributed to their inherent resistance to degradation due to aggregation and age-related declines in clearance mechanisms [32, 33]. To identify proteins that accumulate with age, we performed semi-quantitative mass spectrometry analysis using tandem mass tag (TMT) labeling. Whole brains from young and aged mice were lysed with phase transfer surfactant (PTS) buffer (0.5% deoxycholic acid and 0.33% sarkosyl), which increases the solubility of hydrophobic proteins and enhances their trypsin digestion [34]. The PTS-soluble supernatant, containing most of the brain proteome (Fig S1), was subjected to TMT-based proteomic analysis (Fig 1B). We identified 45 proteins that significantly increased by more than 1.2-fold in the aged mouse brains compared to young mouse

144 brains (S2 Table). Finally, we narrowed down nine proteins showing an age-dependent
145 increase in both proteomic analyses (Fig 1C).

146 To elucidate the characteristics of these proteins enriched in both proteomic analyses, we
147 performed gene ontology analysis (Fig 1D). The term "hyaluronic acid binding" was
148 significantly enriched, encompassing aggrecan core protein (ACAN), hyaluronan and
149 proteoglycan link protein (HAPLN) 1, HAPLN2, and versican core protein (VCAN),
150 which were previously reported to increase with age in rodent brains [35–37]. Therefore,
151 we focused on these proteins as candidates for proteins that aggregate and accumulate
152 with age.

153

154 **Figure 1. Mass Spectrometry Analyses Revealed Sarkosyl-Insoluble Proteins.**
155 Accumulated in Aged Mouse Brains. (A) Workflow (left) illustrating the fractionation of
156 young (2-month-old) and aged (24-month-old) mouse brains to obtain sarkosyl-insoluble
157 protein aggregates. A volcano plot (right) represents the results of label-free quantitative
158 proteomic analysis. The cut-off was set at a false discovery rate (FDR) of 0.01. The
159 colored region in the volcano plot highlights proteins with a fold change > 5.0 and *P*-
160 value < 0.01, as listed in S1 Table. n = 4. Specific proteins are highlighted: ACAN
161 (green), HAPLN1 (orange), HAPLN2 (red), and VCAN (blue). (B) Tandem mass tag
162 (TMT)-based mass spectrometry analysis of phase transfer surfactant (PTS)-soluble
163 supernatant from young (2-month-old) and aged (24-month-old) mouse brains. The cut-
164 off was set at FDR = 0.01. The colored regions in the volcano plots highlight proteins
165 with a fold change > 1.2 and *P*-value < 0.05, as listed in S2 Table. n = 4. (C) A list of
166 proteins significantly increased in both proteomic analyses described in (A) and (B). (D)
167 Bar chart showing gene ontology (GO) terms in the molecular function category enriched
168 among the proteins identified in (C). GO enrichment analysis was performed using the
169 Database for Annotation, Visualization, and Integrated Discovery (DAVID). Proteins
170 included in the enriched categories are indicated on the right side of the chart.

171

172 **HAPLN1 and HAPLN2 formed salkosyl-insoluble protein assemblies in aged mouse**
173 **brains**

174 To validate the proteomic findings, we performed immunoblotting on each fraction
175 prepared as shown in Figure 1A. Consistent with the proteomic analyses, marked age-
176 dependent increases in ACAN, HAPLN1, and HAPLN2 were observed in the sarkosyl-
177 insoluble P2 fraction, while we were unable to assess VCAN due to a lack of detectable
178 antibodies (Figs 2A and 2B). As expected from previous studies, ubiquitinated proteins
179 also increased in the P2 fraction with age (Figs 2A and 2B), confirming the successful
180 enrichment of protein aggregates [35]. These results also demonstrated the sarkosyl-
181 insolubility of ACAN, HAPLN1, and HAPLN2 in aged mouse brains.

182 Characteristics of protein aggregates include not only detergent-insolubility but also the
183 formation of high-molecular-weight assemblies trapped on nitrocellulose membranes and
184 aberrant localization as large deposits *in vivo* [36, 37]. Therefore, we performed a series
185 of experiments to determine whether ACAN, HAPLN1, and HAPLN2 are aggregated in
186 aged mouse brains.

187 First, to investigate whether ACAN, HAPLN1, and HAPLN2 form sarkosyl-insoluble
188 large protein assemblies and are trapped on a nitrocellulose membrane, we performed a
189 filter trap assay using the S1 fraction. The proteins that passed through the nitrocellulose
190 membranes were trapped by the PVDF membrane layered underneath. HAPLN1 and
191 HAPLN2 trapped on the nitrocellulose membrane showed a marked increase with age. In
192 contrast, the amount of ACAN trapped on nitrocellulose membranes did not differ
193 between young (3-month-old) and aged (21-month-old) mice (Fig 2C). The amounts of
194 ACAN, HAPLN1, and HAPLN2 captured in the PVDF membrane were all increased in
195 the S1 fractions of aged mice. These results suggest that HAPLN1 and HAPLN2 formed
196 sarkosyl-insoluble large protein complexes with age, whereas ACAN did not.

197 ACAN, HAPLN1, and HAPLN2 are known to form the extracellular matrix through non-
198 covalent association with hyaluronic acid. A previous study showed that ACAN extracted
199 from the aged mouse brain was enriched in the Triton X-100-insoluble fraction but was
200 solubilized by degrading high-molecular-weight hyaluronic acid. [38]. Therefore, we next

201 investigated whether treatment with hyaluronidase solubilizes ACAN, HAPLN1, and
202 HAPLN2 from the sarkosyl-insoluble P2 fraction. We treated the sarkosyl-insoluble P2
203 fraction with hyaluronidase, followed by ultracentrifugation to yield the supernatant
204 hyaluronidase-extractable S3 and the pellet hyaluronidase-resistant P3 fraction (Fig 2D).
205 ACAN was recovered in the S3 fraction after hyaluronidase treatment (Fig 2E). In
206 contrast, the majority of HAPLN1 and HAPLN2 remained in the P3 fraction, with only a
207 portion shifting to the S3 fraction (Fig 2E). We also performed a filter trap assay on the
208 S3 and P3 fractions. HAPLN1 and HAPLN2 in the P3 fraction were captured on a
209 nitrocellulose membrane, whereas ACAN in the P3 fraction was not captured on a
210 nitrocellulose membrane (Fig 2F). These results suggest that HAPLN1 and HAPLN2
211 form high molecular weight protein assemblies that remain insoluble in sarkosyl despite
212 hyaluronic acid degradation. We focused on HAPLN2 for further investigation because
213 HAPLN2 showed the highest fold change of the nine proteins in both proteomic analyses
214 (Fig 1C).

215

216 **Figure 2. Extracellular Matrix Component Proteins Accumulate in the Sarkosyl-**
217 **Insoluble Fraction of Mouse Brains with Age.** (A) Immunoblot analyses of ACAN,
218 HAPLN1, HAPLN2, and ubiquitin in the S1, P1, S2, and P2 fractions, as outlined in
219 Figure 1A, from mouse brains. n = 2. (B) Densitometric quantitation of (A). The
220 expression levels of the indicated proteins were normalized to α-tubulin in the S1
221 fractions. Error bars represent mean ± S.D. *P*-values by Student's *t*-test. n = 4. (C) Filter
222 trap assay and immunoblot analysis of the S1 fraction from young (3-month-old) and
223 aged (21-month-old) mouse brains. n = 2. (D) Diagram illustrating hyaluronidase
224 treatment of the sarkosyl-insoluble P2 fraction. The P2 fraction was treated with
225 hyaluronidase and centrifuged at 100,000 × *g*. (E) Immunoblot analyses of ACAN,
226 HAPLN1, and HAPLN2 in the hyaluronidase-extractable S3 and hyaluronidase-resistant
227 P3 fractions from 27-month-old mouse brains. n = 3. (F) Filter trap assay of the fractions
228 described in (E). n = 3.

229

230 **HAPLN2 was deposited in the extracellular space in the cerebellar white matter of**
231 **aged mice**

232 To investigate whether HAPLN2 forms aberrant deposits in aged mouse brains, we
233 examined the distribution and morphological structure of HAPLN2 in mouse brains.
234 Previous studies have shown that HAPLN2 is expressed in the cerebellar white matter of
235 young adult mice [39]. Immunoblot analysis confirmed that the HAPLN2 protein was
236 predominantly detected in the cerebellum of 24-month-old mice, whereas it was only
237 faintly detected in the cerebellum of 4-month-old mice (Fig 3A). Immunohistochemical
238 analysis revealed that the expression of HAPLN2 increased with age in the cerebellar
239 white matter, which is mainly composed of myelinated axons expressing myelin basic
240 protein (MBP) and is surrounded by granular layers stained with 4',6-diamidino-2-
241 phenylindole (DAPI) (Fig 3B). These results demonstrate that HAPLN2 accumulates in
242 the cerebellar white matter of aged mice.

243 We next examined its detailed structure in the cerebellar white matter of aged mice.
244 Immunohistochemistry analysis showed significantly enlarged puncta of HAPLN2 in the
245 aged mouse brains compared to young mouse brains (Figs 3C and 3D). We then
246 investigated whether the HAPLN2 deposits are localized to the intracellular or
247 extracellular space. Hyaluronic acid is a major component of the extracellular matrix,
248 which is visualized by staining with hyaluronic acid binding protein (HABP). In young
249 mouse samples, HABP staining was weak, and colocalization of HAPLN2 and HABP
250 was unclear. In contrast, in aged mouse brains, both HABP and HAPLN2 staining
251 showed significantly enlarged puncta, and colocalization of HAPLN2 and HABP was
252 clearly observed (Figs 3E–G, and S2A). These results indicate that HAPLN2 accumulates
253 as large deposits with hyaluronic acid in the extracellular space of the cerebellar white
254 matter of aged mice.

255 To determine which cells in the cerebellum express HAPLN2 and whether the
256 accumulation of HAPLN2 is due to increased mRNA expression or not, we referred to
257 the results of a previous single-cell transcriptome analysis. This data revealed that *Hapln2*
258 mRNA expression was specifically detected in oligodendrocytes and that mRNA levels

259 remained constant between 2–3 months and 21–22 months of age (Fig 3H) [40]. These
260 results suggest that the age-dependent accumulation of HAPLN2 protein is not due to the
261 induction of mRNA expression.

262 Since the single-cell RNA-seq result indicate that HAPLN2 is expressed in
263 oligodendrocytes, we performed co-staining of HAPLN2 and the oligodendrocyte marker
264 MBP [41]. However, the HAPLN2 deposits did not colocalize with oligodendrocytes (Fig
265 3I). We also examined co-staining of HAPLN2 with ubiquitin or p62, since protein
266 aggregates that forms intracellular aggregation and then are deposited extracellularly, as
267 is typically observed with tau, often colocalize with these proteins [42]. However,
268 HAPLN2 did not colocalize with ubiquitin and p62 (Figs S2B and S2C). These results
269 suggest that HAPLN2 is secreted from oligodendrocytes and then accumulated in the
270 extracellular space.

271 We next investigated whether enlarged HAPLN2 puncta retain their physiological
272 function. HAPLN2 is normally localized to the perinodal extracellular matrix, which
273 surrounds the nodes of Ranvier and contains hyaluronic acid [43]. Therefore, we
274 examined the colocalization between HAPLN2 and contactin-associated protein (Caspr),
275 which localizes to the nodes of Ranvier. The colocalization of HAPLN2 with Caspr
276 decreased with age (Figs 3J and 3K). In addition, Mander's overlap coefficient (MOC)
277 M1, which indexes the proportion of HAPLN2 colocalized with Caspr, decreased with
278 age (Fig 3L), suggesting that HAPLN2 was abnormally localized outside the nodes of
279 Ranvier in aged mice. In contrast, MOC M2, an index of the proportion of Caspr
280 colocalized with HAPLN2, did not change with age (Fig 3M), suggesting that most of
281 Caspr colocalizes with functional HAPLN2 and that the nodes of Ranvier are not
282 dysregulated in aged mice. Additionally, the area of HAPLN2 mislocalized from Caspr
283 was larger than HAPLN2 colocalized with Caspr in 24-month-old mice (Fig 3N). This
284 further supports that enlarged HAPLN2 puncta have lost their function.

285

286 **Figure 3. HAPLN2 Forms Aggregate-Like Structures in the Cerebellar White**
287 **Matter of Aged Mice.** (A) Immunoblot analysis of the S1 fraction from the cerebrum

288 and cerebellum of mice. n = 2. (B) Representative images of fluorescence
289 immunohistochemistry of the mouse cerebellum showing HAPLN2, myelin basic protein
290 (MBP, a marker for myelinated axons), and 4',6-diamidino-2-phenylindole (DAPI). n = 3.
291 (C) Magnified fluorescence immunohistochemistry images for HAPLN2 corresponding
292 to the boxed areas in the left panels. n = 3. (D) Quantitation of the area of each HAPLN2-
293 positive punctum in (C). (E) Representative images of fluorescence
294 immunohistochemistry for HAPLN2 and biotinylated hyaluronic acid-binding protein
295 (HABP), a probe for hyaluronic acid. n = 3. (F) Quantitation of the area of each HABP-
296 positive punctum. (G) Pearson's correlation coefficients for colocalization between
297 HAPLN2 and HABP. (H) Single-cell transcriptomics data from Ximerakis et al., *Nat*
298 *Neurosci* (2019). TPM: transcripts per million. ASC: astrocyte; MG: microglia; NEUR:
299 mature neuron; OLG: oligodendrocyte. Error bars indicate maximum values, boxes
300 indicate the first and third quartiles, and solid and dashed lines represent the median and
301 mean, respectively. (I) Representative images of fluorescence immunohistochemistry for
302 HAPLN2 and MBP as an oligodendrocyte marker in the cerebellar white matter. n = 3.
303 (J) Representative images of fluorescence immunohistochemistry for HAPLN2 and
304 Caspr, a marker for the nodes of Ranvier. n = 3. (K–M) Colocalization analysis between
305 HAPLN2 and Caspr using Pearson's correlation coefficient (K) and Mander's overlap
306 coefficients (MOC) M1 (L) and M2 (M). MOC M1 represents the proportion of HAPLN2
307 overlapping Caspr, while MOC M2 represents the reverse. (N) Quantitation of the area of
308 each HAPLN2 punctum, categorized by whether it merges with Caspr in 24-month-old
309 mice. All coefficient calculations were performed using ImageJ (version 1.53t) with the
310 JACoP plugin. Scale bars: 1 mm (B and C (left)) and 10 μm (C (right); E; I; J). Error bars
311 represent mean ± S.D. *P*-values by Student's *t*-test.

312

313 **Deposition of HAPLN2 aggregates starts in middle age in mouse brains**

314 Research in humans and rodents has highlighted middle age as a period marked by the
315 onset of changes associated with brain aging [44]. To investigate whenHAPLN2 starts to
316 accumulate, we examined the age-related progression of HAPLN2 accumulation in the

317 mouse brain. We performed sarkosyl fractionation followed by immunoblot analysis
318 using young (3- and 6-month-old), middle-aged (12-month-old), and aged (18-month-old)
319 mice. HAPLN2 began to accumulate in the S1 and P2 fractions from 12-month-old mice
320 and was further enriched in 18-month-old mice (Fig 4A). Correspondingly, the puncta of
321 HAPLN2 became larger in 12- and 18-month-old mice, consistent with the immunoblot
322 analysis (Figs 4B and 4C). These results indicate that HAPLN2 accumulates gradually
323 from middle age to old age, further confirming the age-dependent accumulation of
324 HAPLN2 aggregates.

325

326 **Figure 4. Time-Course Analysis of Age-Dependent HAPLN2 Accumulation in**
327 **Mouse Brains.** (A) Immunoblot analyses of the S1 and P2 fractions from the mouse
328 cerebellum at different ages. n = 3. (B) Representative images of fluorescence
329 immunohistochemistry of the mouse cerebellum showing HAPLN2 and DAPI staining. n
330 = 3. (C) Quantitation of the area of each HAPLN2-positive structure shown in (B). Error
331 bars represent mean ± S.D. *P*-values by one-way ANOVA followed by Tukey's *post hoc*
332 test.

333

334 **Low pH, high NaCl concentration, and hyaluronic acid promoted HAPLN2**
335 **aggregation**

336 To investigate the factors affecting HAPLN2 aggregation, we explored the aggregation
337 propensity of recombinant HAPLN2 protein. Various factors have been reported to
338 influence the formation of protein aggregates, including pH and NaCl concentration. For
339 instance, the TAR DNA-binding protein of 43 kDa (TDP-43) aggregates at high pH and
340 NaCl concentration [45], while fused in sarcoma (FUS) aggregates at low concentrations
341 of RNA [46] and in the presence of dextran [47, 48] and NaCl [49]. Therefore, we
342 incubated recombinant HAPLN2 protein in buffers with varying pH and NaCl
343 concentration, and in the presence or absence of hyaluronic acid. The formation of
344 amorphous aggregates of HAPLN2 was promoted at low pH, high NaCl concentration,

345 and in the presence of hyaluronic acid (Figs 5A, 5B, S3A, and S3B). Quantitative area
346 measurements revealed that recombinant HAPLN2 formed amorphous aggregates larger
347 than 10 μm^2 at pH 6.0, while it formed small oligomer-like aggregates less than 10 μm^2
348 at pH 7.0, and no aggregates were formed at pH 8.0 in 150 mM NaCl (Fig S3C).
349 Transmission electron microscopy analysis further confirmed that HAPLN2 incubated at
350 pH 6.0 in 150 mM NaCl formed amorphous aggregates (Fig S3D).

351 Many protein aggregates contain cross-β-sheet structures and form protein fibrils.
352 However, it is impossible to distinguish between oligomeric and fibrillar structures using
353 diffraction-limited optics [50]. To examine whether HAPLN2 aggregates contain β-sheet-
354 mediated aggregates that are stained with thioflavin T or Nile Red, we conducted super-
355 resolution imaging analysis (Fig S3E) [51]. In recombinant HAPLN2 incubated at pH
356 6.0, some spots, but not the entire aggregate, were stained with thioflavin T and Nile Red,
357 indicating that the amorphous-appearing HAPLN2 aggregates contain cross-β-sheet
358 structures (Fig 5C).

359 To analyze whether the HAPLN2 aggregates formed fibrillar structures, which are
360 characterized by a long axis and low circularity ratio, we statistically analyzed the
361 morphology of the Nile Red-positive clustered aggregates, according to a previous report
362 [52]. The long axis of the Nile Red-positive clusters increased under acidic conditions
363 (Fig 5D), but the circularity ratio did not change with pH (Fig 5E). These results suggest
364 that low pH induces the formation of amorphous, rather than fibrillar, aggregates of
365 HAPLN2 containing partial cross-β-sheet structures.

366

367 **Figure 5. Aggregates of Recombinant HAPLN2 Formed Under Low pH, High NaCl,**
368 **or Hyaluronic Acid Conditions Partially Contain Cross-β-Sheet Structures.** (A)
369 Brightfield microscopic images of recombinant HAPLN2 aggregates incubated in the
370 indicated buffer conditions without agitation. (B) Phase diagrams showing the
371 aggregation states of recombinant HAPLN2 under the indicated buffer conditions. (C)
372 Brightfield and highly inclined and laminated optical sheet (HiLo) images of recombinant
373 HAPLN2 aggregates incubated in a buffer at the indicated pH with 150 mM NaCl.

374 Thioflavin T and Nile Red were used at concentrations of 5 μM and 5 nM, respectively to
375 visualize cross-β-sheet structures. (D, E) Quantitative analyses of the long axis (D) and
376 circularity ratio (E) of Nile Red-positive aggregates shown in (C). Data were collected
377 from at least five fields of view. 500 nM Recombinant HAPLN2 monomers were
378 incubated for 24 hours at 37ºC in all conditions. Error bars represent mean ± S.D. *P*-
379 values by one-way ANOVA followed by Tukey's *post hoc* tests. Scale bars: 10 μm (A), 1
380 μm (C).

381

382 **Treatment with hyaluronidase promoted the clearance of HAPLN2 aggregates in**
383 **the mouse cerebellar white matter**

384 It has been reported that the volume of the extracellular spaces reduces with age, which is
385 thought to lead to impairment of protein aggregate clearance [53, 54]. Hyaluronic acid is
386 the major component of the perinodal extracellular matrix and accumulate in the brain
387 with aging [55–59]. Furthermore, it has been shown that hyaluronidase treatment
388 increases the volume of the extracellular space in mouse hippocampal slices [60].
389 Therefore, we hypothesized that reducing hyaluronic acid would increase the
390 extracellular space and improve access to HAPLN2 aggregates, thereby enhancing the
391 clearance of HAPLN2 aggregates.

392 To test this idea, we injected hyaluronidase into the mouse cerebellum (Fig 6A).
393 Immunohistochemical analysis revealed that the expression and size of HAPLN2
394 dramatically decreased 16 hours after hyaluronidase injection (Figs 6B and 6C).
395 Immunoblot analysis of brain lysates fractionated as in Figure 1A showed that HAPLN2
396 in the sarkosyl-insoluble P2 fractions in the hyaluronidase-injected brain (ipsilateral)
397 significantly decreased compared to that in the PBS-injected ipsilateral brain, whereas
398 HAPLN2 levels in the sarkosyl-soluble S2 fractions were not significantly affected (Figs
399 6D and 6E). These results suggest that hyaluronidase specifically promoted the clearance
400 of aggregated HAPLN2.

401

402 **Figure 6. Hyaluronidase Promotes Clearance of HAPLN2 Aggregates in the Mouse**
403 **Cerebellum.** (A) Schematic illustration of hyaluronidase injection into the mouse
404 cerebellum. (B) Fluorescence immunohistochemistry images of the cerebellum of 12-
405 months-old mice showing HAPLN2, HABP, and DAPI signals. n = 4. (C) Quantitation of
406 the area of HAPLN2-positive puncta in (B). (D) Immunoblot analysis of the cerebellum
407 corresponding to the samples in (B). (E) Densitometric quantification of (D). HAPLN2
408 Protein levels in the S2 fraction were normalized to α-tubulin in the S2 fractions.
409 HAPLN2 Protein levels in the P2 fraction were normalized to α-tubulin in the S1
410 fractions. Error bars represent mean ± S.D. *P*-values by one-way ANOVA followed by
411 Tukey's *post hoc* tests.

412

413 **Microglia regulated the accumulation of HAPLN2 aggregates**

414 Microglia are the resident macrophages in the brain, acting as scavengers that remove
415 debris and protein aggregates from the extracellular space through phagocytosis [61]. To
416 examine whether microglia are involved in the clearance of HAPLN2 aggregates, we
417 treated 4-week-old mice with pexidartinib (PLX3397), a colony-stimulating factor 1
418 receptor (CSF1-R) inhibitor known to deplete microglia [62]. Immunostaining with
419 ionized calcium-binding adapter molecule 1 (Iba1), a microglia/macrophage marker,
420 confirmed that treatment with PLX3397 for two months successfully depleted microglia
421 (Fig 7A). Immunohistochemical analysis showed that microglial depletion resulted in the
422 accumulation and enlargement of HAPLN2 puncta in the brains of PLX3397-treated mice
423 (Figs 7B and 7C). Furthermore, PLX3397 treatment resulted in HAPLN2 enrichment
424 within the sarkosyl-insoluble fraction of the cerebellum (Figs 7D and 7E). These results
425 suggest that microglia play a critical role in the clearance of HAPLN2 aggregates.

426

427 **Figure 7. Accumulation of HAPLN2 Aggregates Is Promoted by Microglial**
428 **Depletion in the Cerebellum.** (A) Immunohistochemistry images of the cerebellum from
429 mice fed AIN-76A control chow or AIN-76A containing 290 mg/kg PLX3397 from one

430 month to three months of age, stained with anti-ionized calcium-binding adaptor
431 molecule 1 (Iba1) antibody as a microglia marker. n = 3. (B) Immunohistochemistry
432 images of the cerebellum from the mice in (A), stained with anti-HAPLN2 antibody. n =
433 3. (C) Quantification of the area of each HAPLN2-positive punctum in (B). (D)
434 Immunoblot analysis of the cerebellum from the mice in (B), fractionated as described in
435 Figure 1A. n = 3. (E) Densitometric quantitation of (D). Protein expression levels were
436 normalized to α-tubulin in the S1 fractions. Error bars represent mean ± S.D. *P*-values
437 were calculated using Student's *t*-test.

438

439 **Oligomers and aggregates of HAPLN2 induced microglial activation *in vitro* and *in***
440 ***vivo***

441 Microglia that phagocytose extracellular protein aggregates exhibit a pro-inflammatory
442 M1 phenotype and secrete cytokines such as interleukin (IL)-6 and tumor necrosis factor
443 (TNF)-α [61]. Recent studies have shown that soluble oligomers of Aβ, tau, and α-
444 synuclein in the extracellular spaces induce inflammatory responses prior to the
445 accumulation of protein aggregates in the brains of patients with neurodegenerative
446 diseases [63].

447 To investigate whether HAPLN2 triggers microglial inflammation, we purified
448 recombinant proteins of full-length HAPLN2 and each domain from a lipopolysaccharide
449 (LPS)-free *Escherichia coli* strain (Fig. 8A). The N-terminal Ig-like domain is thought to
450 mediate protein interactions, while the Link1 and Link2 domains are believed to bind to
451 hyaluronic acid. First, we performed a filter trap assay to determine whether solubilized
452 full-length HAPLN2 and the N-terminal Ig-like domain exist as monomers or soluble
453 oligomers. Both soluble full-length HAPLN2 and the N-terminal Ig-like domain were
454 trapped on the nitrocellulose membrane after ultracentrifugation, indicating that they
455 form soluble oligomers (Fig. S4A). We also prepared aggregated full-length HAPLN2
456 and the N-terminal Ig-like domain by incubating soluble each soluble protein at pH 6.0,
457 which was confirmed by filter trap assay (Fig. S4A).

458 To evaluate the potential to induce microglial inflammatory responses, we added full-
459 length HAPLN2 oligomers and aggregates as well as the positive control LPS to the MG6
460 microglial cell line. Both soluble oligomers and aggregates of HAPLN2 increased the
461 mRNA expression of IL-6 and TNF-α (Fig. 8B). These results suggest that HAPLN2
462 induces pro-inflammatory microglial activation in both the soluble oligomeric and
463 aggregated states.

464 To determine whether specific domains of HAPLN2 induce pro-inflammatory microglial
465 activation, we added soluble full-length HAPLN2 and its individual domains to MG6
466 cells. Soluble OxStayGold fluorescent protein, which was not trapped by the
467 nitrocellulose membrane, was used as a negative control (Fig S4A). Soluble full-length
468 HAPLN2 significantly induced IL-6 and TNF-α mRNA expression, but none of the
469 individual domains of HAPLN2 upregulated these cytokines (Fig 8C). These results
470 suggest that the pro-inflammatory effect is associated with full-length HAPLN2 and not
471 with specific domains.

472 Finally, we examined whether HAPLN2 oligomers induce microglial activation in mouse
473 brains by infusing full-length HAPLN2 and each domain into the hippocampus. Injection
474 of full-length HAPLN2 increased pro-inflammatory microglia, marked by Iba1, in the
475 hippocampus (Figs 8E, F, and S4B). In contrast, oxStayGold and each domain of
476 HAPLN2 did not significantly induce microglial activation, consistent with Figure 8C.
477 These results suggest that oligomeric full-length HAPLN2 promotes microglial activation
478 *in vivo*.

479

480 **Figure 8. HAPLN2 Induced Microglial Activation *In Vitro* and *In Vivo*. (A) Diagram**
481 **of the domains within HAPLN2.** (B) Reverse transcription polymerase chain reaction
482 (RT-qPCR) analysis of pro-inflammatory cytokine mRNA (*Il6* and *Tnf*, normalized to
483 *Actb*) in MG6 cells stimulated with 1 μM LPS, and 200 nM recombinant full-length
484 HAPLN2 in soluble and aggregated states for four hours. PBS served as a control.
485 Recombinant HAPLN2 was aggregated by incubation in a buffer containing 10 mM
486 sodium phosphate and 300 mM NaCl (pH 6.0) for 24 hours at 37ºC. (C) RT-qPCR

487 analysis of pro-inflammatory cytokine mRNA (*Il6* and *Tnf*, normalized to *Actb*) in MG6
488 cells stimulated with 1 μM LPS, and 200 nM of recombinant proteins (oxStayGold, full-
489 length HAPLN2, HAPLN2 Ig-like domain, HAPLN2 link 1 domain, and HAPLN2 link 2
490 domain) for four hours. PBS served as a control. (D) Fluorescence immunohistochemistry
491 images of the hippocampus of three-months-old mice injected with PBS, 20 μg LPS, and
492 15 pmol of recombinant proteins (oxStayGold, full-length HAPLN2, HAPLN2 Ig-like
493 domain, HAPLN2 link 1 domain, and HAPLN2 link 2 domain). The brains were stained
494 with anti-Iba1 antibody to detect activated microglia. Scale bar, 500 μm. n = 4. (E)
495 Quantitation of the number of activated microglia labeled by Iba1 from (E). Error bars
496 represent mean ± S.D. *P*-values were calculated using one-way ANOVA followed by
497 Tukey's *post hoc* tests.

498

499 **HAPLN2 accumulated with age in the human cerebellum**

500 Finally, we examined whether HAPLN2 accumulates with age in the human brain. We
501 stained HAPLN2 in the cerebellum of human brains in their sixties or eighties without
502 dementia (S3 Table). We observed the increased HAPLN2 puncta in the human brain in
503 their eighties compared to those in their sixties (Fig 9A). These HAPLN2 puncta did not
504 colocalize with Caspr, suggesting that these are age-dependent aggregates. In addition,
505 the area of HAPLN2 puncta increased with age (Figs 9B and 9C). These results suggest
506 that HAPLN2 accumulation is a common hallmark of aging in both mice and humans.

507

508 **Figure 9. HAPLN2 Formed Large Puncta with Age in the Human Cerebellum.** (A)
509 Fluorescent immunohistochemistry images for HAPLN2, Caspr, and DAPI in the
510 cerebellum from human post-mortem brains without dementia. Scale bar, 50 μm. (B)
511 Quantification of the area of each HAPLN2 puncta in (A). (C) Quantification of the
512 average area of HAPLN2 puncta across all samples in (A). Error bars represent mean ±
513 S.D. *P*-values were calculated using Student's *t*-test.

514

515 # Discussion

516 Research on age-related protein aggregation in mammals has progressed at a slower pace
517 than that in *C. elegans* due to the difficulty in obtaining a sufficient number of aging
518 individuals. Recently, studies have aimed to identify proteins that become Triton X-100
519 insoluble in cerebral cortex with age [64]. However, as demonstrated by the evidence that
520 membraneless organelle constituent proteins and functional large protein complexes, such
521 as the cytoskeleton, also become Triton X-100 insoluble, these proteins are not
522 synonymous with aggregated proteins[64]. Therefore, we used sarkosyl to search for
523 proteins that aggregate with aging under conditions that fractionate Aβ and tau protein
524 aggregates.

525 We identified nine proteins that become sarkosyl-insoluble and accumulate in mouse
526 brains with aging. Of these, seven were extracellular matrix components,
527 immunoglobulin components, and cell adhesion factors, all of which are localized
528 extracellularly or are in contact with the extracellular space. We focused on HAPLN2, a
529 component of the perinodal extracellular matrix, as a protein that aggregates in an age-
530 dependent manner. HAPLN2 aggregates colocalized with hyaluronic acid in the
531 cerebellum white matter (Fig 3D). This observation, coupled with the *in vitro* finding that
532 hyaluronic acid promotes aggregation of HAPLN2 (Fig 5A), suggests a key role for
533 hyaluronic acid in this process. This is consistent with reports that the concentration of
534 hyaluronic acid increases especially in prefrontal cortex and cerebellum with age *in vivo*
535 [55, 59, 65]. Furthermore, it is reported that microglia are fewer in number and more
536 sparsely distributed in the cerebellum compared to other brain regions [66–68].
537 Therefore, clearance of protein aggregates by microglial phagocytosis may be less
538 efficient in the cerebellum compared to the cerebrum. Moreover, the cerebellum has a
539 significantly higher density of neurons and axons compared to the cerebrum [69]. This
540 implies a greater number of nodes of Ranvier and their associated perinodal extracellular
541 matrix, which could contribute to the high expression of HAPLN2 observed in this
542 region. This may explain the significant HAPLN2 aggregation observed in the
543 cerebellum.

544 Experiments using recombinant HAPLN2 revealed that the formed amorphous aggregates
545 partially contained cross-β-sheet structures, characteristic of proteinaceous aggregates
546 (Fig 5C). This suggests that HAPLN2 forms aggregates through protein-protein
547 interactions, rather than simply forming complexes with hyaluronic acid. Interestingly,
548 HAPLN2 extracted from the sarkosyl-insoluble P2 fraction of aged mouse brains
549 remained insoluble even after enzymatic degradation of hyaluronic acid (Figs 2D and
550 2E). This suggests that while initial aggregation may be driven by interactions with
551 hyaluronic acid, HAPLN2 aggregates ultimately acquire protein-protein interactions that
552 maintain sarkosyl insolubility. Adding another layer to the role of hyaluronic acid, we
553 also showed that injecting hyaluronidase into the mouse cerebellum led to a decrease in
554 sarkosyl-insoluble HAPLN2. Hyaluronidase treatment may increase the accessibility of
555 clearance systems, such as microglia or the glymphatic system, by increasing the volume
556 of extracellular spaces [60]. This is supported by studies showing that increased
557 extracellular volume enhances Aβ clearance [70]. Hence, manipulating hyaluronic acid
558 levels may be a viable approach to modulate HAPLN2 aggregation by influencing
559 extracellular volume and the accessibility of clearance mechanisms. However, further
560 research is needed to determine whether microglia or the glymphatic system are
561 responsible for the enhanced clearance of HAPLN2 aggregates following hyaluronidase
562 injection. Additionally, recombinant HAPLN2 protein efficiently formed aggregates
563 under low pH conditions (Fig 5). Given that brain pH decreases with age, from 6.30 to
564 6.00 in humans and from 6.85 to 6.70 in mice [71], this change in the brain environment
565 may also contribute to HAPLN2 aggregation. Taken together, our data suggest that
566 changes in brain pH and hyaluronic acid levels may contribute to the aggregation of
567 HAPLN2 *in vivo*, highlighting the complex interplay between protein aggregation and the
568 aging brain environment, particularly for HAPLN2.

569 Microglia play a critical role in clearing extracellular waste, such as protein aggregates,
570 through phagocytosis [61]. Recent studies have also shown that microglia phagocytose
571 the extracellular matrix, including the perineuronal net [72, 73]. However, aging is
572 associated with a decline in microglial phagocytic capacity due to increased expression of
573 CD22, a negative regulator of phagocytosis [11, 74]. Our study demonstrated that

574 microglial depletion promotes the accumulation of HAPLN2 aggregates (Fig 7),
575 suggesting that age-related impairment of microglial phagocytosis disrupts the clearance
576 of HAPLN2 and the perinodal extracellular matrix. The accumulation of protein
577 oligomers and aggregates in the extracellular space activates microglia. This leads to the
578 secretion of pro-inflammatory cytokines, such as IL-6 and TNF-α, which contribute to
579 chronic inflammation [75]. Our study showed that excessive HAPLN2 oligomers and
580 aggregates activate microglia both *in vitro* and *in vivo* (Fig 8). These findings indicate
581 that while microglia are involved in clearing HAPLN2 aggregates, their phagocytic
582 capacity can become overwhelmed by abnormal accumulation of HAPLN2 aggregates.
583 This imbalance may trigger microglial pro-inflammatory activation, further contributing
584 to chronic inflammation, a key feature of brain aging. Additionally, aging is associated
585 with a decline in cerebrospinal fluid perfusion, impairing the clearance of extracellular
586 waste by the glymphatic system [12]. This decline may exacerbate the accumulation of
587 HAPLN2 aggregates and further promote neuroinflammation in aged brains. However,
588 further research is needed to elucidate the mechanism linking the glymphatic system with
589 accumulation of HAPLN2 aggregates and neuroinflammation during aging.

590 In summary, we have identified HAPLN2, a component of the perinodal extracellular
591 matrix, as an age-dependent protein aggregate. HAPLN2 aggregates mislocalize and
592 accumulate in the extracellular space in aged mouse brains, where hyaluronic acid and
593 microglia regulate their accumulation and clearance. We also observed HAPLN2
594 aggregates in non-demented human brains. Our study suggests HAPLN2 aggregation as
595 a potential factor in chronic inflammation in the brain during physiological aging and
596 sheds new light on our understanding of age-related decline in brain function.

597

598 # Materials and Methods

599 ## Post-mortem brain samples

600 The paraffin-embedded postmortem cerebellum derived from neurologically normal
601 patients in their sixties (n = 4) or eighties (n = 5) were obtained from Japan Brain Bank

602 Net (JBBN). Information on human donors is provided in S3 Table. All participants,
603 before passing away or their families, provided written informed consent. Experiments
604 using human samples were performed with institutional approval and guidelines from the
605 institutional ethical committee of the Graduate School of Pharmaceutical Sciences,
606 University of Tokyo (No. 4-8).

607

608 Animals

609 C57BL/6N mice were purchased from Clea Japan. All mice were maintained under
610 specific pathogen-free conditions. All animal experiments were performed after obtaining
611 approval from the Institutional Animal Care Committee of the Graduate School of
612 Pharmaceutical Sciences, the University of Tokyo (approval number P26-7). Male mice
613 were used in all experiments. Mice were euthanized by cervical dislocation to preserve
614 the metabolic environment of the brains and to prevent artifacts that could alter the
615 biochemical profiles of the proteome. Mouse brains were bisected down the midline to
616 yield two hemispheres. The brain hemisphere of each animal was quickly frozen on dry
617 ice and stored at -150ºC until use.

618

619 Cell culture

620 The MG6 cell line is a c-Myc-immortalized cell line of mouse microglia. MG6 cells were
621 maintained at 5% CO_2 at 37ºC in Dulbecco's modified Eagle's medium supplemented
622 with 10% (v/v) fetal bovine serum (Thermo Fisher Scientific, 10270-106), 10 µg/mL
623 insulin (Nacalai Tesque, 12878-44), and 0.1 mM 2-mercaptoethanol [76, 77].

624

625 Label-free quantitative proteomic analysis

626 The fractionation of the brain tissues was prepared as previously described [30]. Tissues
627 were crushed using Multi-Beads-Shocker (Yasui Kikai, MB601U(S)). Then the tissues
628 were homogenized with a Potter-type homogenizer (AS ONE CORPORATION) at 800
629 rpm in 1.4 mL of sarkosyl buffer [PBS, 1% sarkosyl (Nacalai Tesque, 20135-14) and 1
630 mM phenylmethylsulfonyl fluoride (PMSF) (Wako, 020-15372)]. The homogenates were
631 centrifuged at 15,000 × *g* for 5 minutes twice, then for 15 minutes once at 4ºC to obtain
632 supernatant (S1) and pellet (P1) fractions. The supernatants were centrifuged at 100,000
633 × *g* for one hour at 4ºC to obtain sarkosyl-soluble (S2) and sarkosyl-insoluble (P2)
634 fractions. The P2 fraction was resuspended in 140 µL of phase transfer surfactant PTS
635 [12 mM sodium deoxycholate (SDC), 12 mM sarkosyl, and 200 mM ammonium
636 bicarbonate] buffer. The resuspended P2 solutions were sonicated with Bioruptor® Plus
637 (BMBio, B01020001) for 10 cycles, (30”/30” cycles), and incubated for 30 minutes at
638 60ºC with 5 mM dithiothreitol (DTT) for solubilization and reduction of the proteins. The
639 samples were then alkylated with 200 mM methyl methanethiosulfonate for 30 minutes at
640 room temperature in the dark. The samples were purified with methanol-chloroform
641 extraction and solubilized with 50 µL of Rapigest buffer [0.1% Rapigest SF (Waters,
642 186002123) and 50 mM tetraethylammonium bicarbonate (Thermo Fisher Scientific,
643 90114)]. The alkylated samples were sonicated and were digested overnight with 1 µg of
644 Trypsin Gold (Promega, V5280) at 37ºC. Peptides were purified from the supernatant by
645 GL-tip SDB (GL Sciences, 7820-11200) and eluted with QE-B solution [70%
646 Acetonitrile and 0.1% formic acid] (Kanto Chemical Co. Inc., 01922-64). Peptides were
647 concentrated with Concentrator Plus™ for 45ºC and resuspended with 30 µL of QE-A
648 solution [0.1% formic acid] (Kanto Chemical Co. Inc., 16245-12). The concentration of
649 peptides was measured with Pierce Quantitative Colorimetric Peptide Assay (Thermo
650 Fisher Scientific, 23275). 500 ng of peptides from each fraction were subjected to
651 proteomic analysis using an EASY-nLC 1200 system connected online to Q-Exactive
652 (Thermo Fisher Scientific). Samples were loaded onto Acclaim PepMap 100 C18 column
653 (75 µm × 2 cm, 3 µm particle size and 100 Å pore size; 164946, Thermo Fisher Scientific)
654 and separated using capillary column, (75 µm × 12.5 cm, 3 µm particle size, NTCC-
655 360/75-3-125, Nikkyo Technos) in an EASY-nLC 1200 system (Thermo Fisher
656 Scientific). Data were analyzed using Proteome Discoverer (v.2.4). The mass tolerances

657 for the precursor and fragment ions were 10 ppm and 0.02 Da, respectively, and peptide
658 identification was filtered at a false discovery rate <0.01.

659

660 Tandem-mass tag (TMT) proteomics

661 The TMT proteomics was conducted as described previously [34]. Tissues were crushed
662 and homogenized in 400 μL of PTS buffer. The homogenates were centrifuged at 15,000
663 × *g* for 15 minutes at 4ºC to yield the supernatant and pellet fractions. 30 μg of the
664 supernatant was reduced with 5 mM DTT for 15 minutes at room temperature. The
665 samples were then alkylated and digested by Trypsin Gold. The samples were centrifuged
666 at 15,000 × *g* and the supernatants were labeled with TMT sixplex™ Mass Tag Labeling
667 Kits and Reagents (Thermo Fisher Scientific, 90061). The labeled samples were added
668 with 0.1% trifluoroacetate (Wako, 192-09912), incubated for 45 minutes at 37ºC, and
669 centrifuged at 15,000 × *g* for 15 minutes at 4ºC. The supernatant was fractionated with
670 Pierce High pH Reversed-Phase Peptide Fractionation Kit (Thermo Fisher Scientific,
671 84868). The eluates were concentrated at 45ºC and resuspended with 40 μL of QE-A. 500
672 ng of peptides were centrifuged at 15,000 × *g* for 15 minutes at 4ºC and subjected to
673 proteomic analysis with Q-Exactive.

674

675 GO-term analysis

676 In the GO analysis of proteomic data, we used the Database for Annotation, Visualization
677 and Integrated Discovery (DAVID) [78].

678

679 Antibodies

680 Primary antibodies for immunoblotting (IB) and immunohistochemistry (IHC) are listed
681 in S4 Table. All secondary antibodies used for immunoblotting were purchased from

682 Jackson ImmunoResearch Laboratories: Peroxidase AffiniPure™ Rabbit Anti-Mouse IgG
683 + IgM (H+L) (315-035-048), Peroxidase AffiniPure™ Goat Anti-Rabbit IgG (H+L)
684 (111-035-144), and Peroxidase AffiniPure™ Donkey Anti-Goat IgG (H+L) (705-035-
685 147). All the secondary antibodies used for immunohistochemistry were purchased from
686 ThermoFisher Scientific: Alexa Fluor 488 Goat Anti-Mouse IgG (H+L) (A-28175),
687 Alexa Fluor 488 Goat Anti-Rabbit IgG (H+L) (A-11008), Alexa Fluor 555 Mouse Anti-
688 Mouse IgG (H+L) (A-28180), Alexa Fluor 647 Streptavidin (S21374).

689

690 # Immunoblot analysis

691 Sample preparation, sodium dodecyl sulfate-polyacrylamide gel electrophoresis (SDS-
692 PAGE), and immunoblot analysis were performed as described previously [79]. Each
693 fraction of the brain lysates was mixed with SDS lysis buffer [50 mM Tris-HCl (pH 8.0),
694 150 mM NaCl, 0.1% SDS, 1% Triton X-100, 0.5% SDC, and 1 mM PMSF] and
695 centrifuged at 20,000 × *g* for 20 minutes at 4ºC. The supernatants were separated by
696 SDS-PAGE (12.5% acrylamide, 7 × 8 cm, 1 mm thick). Proteins were electrotransferred
697 to Immobilon®-P polyvinylidene difluoride (PVDF) (Merck Millipore, IPVH00010), at
698 30 V for one hour at room temperature. For immunoblot analysis, the membranes were
699 incubated with Blocking One (Nacalai Tesque, 03953-95) for one hour at room
700 temperature. The membranes were incubated with primary antibodies in TBS-T buffer
701 [20 mM Tris-HCl (pH8.0), 150 mM NaCl, and 0.1% Tween-20] overnight at 4ºC, washed
702 with TBS-T buffer and incubated with horseradish-peroxidase conjugated secondary
703 antibody (1:20,000) for 30 minutes at room temperature. The membranes were immersed
704 with ImmunoLightning Plus (PerkinElmer, NEL105001EA) or ImmunoSTAR LD
705 (Wako, 290-69904), and the images were acquired with FUSION FX7.EDGE (VILBER).
706 For band quantification, the intensity of each band was measured using Fiji software
707 (ImageJ2, version 2.14.0/1.54h) [80].

708

709 # Filter trap assay

710 The S1 fractions of the young and aged mouse brains were serially diluted two-fold with
711 sarkosyl buffer. The 50 µL of each sample were filtered under vacuum through a pre-wet
712 0.45-µm pore size nitrocellulose (Bio-Rad, 1620167) and Immobilon®-P, using a Bio-
713 dot® Microfiltration Apparatus (Bio-Rad, 1706545). Each well was washed three times
714 with the sarkosyl buffer. The membranes were then processed following the same
715 immunoblotting procedure from the blocking step onward.

716

717 Immunohistochemical analysis

718 The paraffin sections (10 µm) were boiled in 10 mM sodium citrate buffer (pH 6.0) for
719 one minute in a microwave oven for heat-induced antigen retrieval. The sections were
720 incubated for one hour in Blocking One Histo (Nacalai Tesque, 06349-64), then
721 overnight at 4ºC with primary antibodies diluted in Blocking One Histo. After rinsing,
722 sections were incubated with secondary antibodies and 1 µg/mL 4',6-diamido-2-
723 phenylindole dihydrochloride (DAPI) (Nacalai Tesque, 11034-56) diluted in Blocking
724 One Histo for one hour at room temperature. The sections were washed by TBS-T three
725 times and by PBS three times, then immersed in TrueBlack® Lipofuscin
726 Autofluorescence Quencher (Biotium Inc., 23007) for 20 minutes to reduce
727 autofluorescence from lipofuscin. The slices were mounted with Prolong™ Glass
728 Antifade Mountant (Invitrogen™, P36980).

729 For the staining of Iba1, TSA plus amplification kit (Akoya Biosciences, NEL741001KT)
730 was used in combination with subsequent conventional immunofluorescence staining for
731 other antigens. To block endogenous peroxidase activity, brain sections were treated with
732 3% H_2O_2 in methanol for 15 minutes at room temperature. After washing, sections were
733 treated with Blocking one Histo for one hour at room temperature, and then incubated
734 with 0.1% anti-Iba1 antibody (Wako, 013-27691) in 5% Blocking one Histo in TBS-T
735 overnight at 4ºC. The sections were incubated with 0.01% Peroxidase AffiniPure™ Goat
736 Anti-Rabbit IgG (H+L) (Jackson ImmunoResearch Laboratories, 111-035-144) diluted in
737 TNB buffer at 4ºC overnight. After washing with TNT buffer (0.1% Triton X-100, 100
738 mM Tris-HCl (pH 7.5), 150 mM NaCl) three times, the sections were reacted with

739 Fluorescein Plus amplification reagent for 10 minutes at room temperature, washed with
740 TNT.

741 Images were captured by BZ-X800 (Keyence) using 100X objectives or Leica DMi8
742 Thunder (Leica Microsystems) using 10X or 63X objectives. The images were processed
743 and analyzed with Fiji software. Colocalization analyses were performed with the JaCoP
744 plugin in Fiji software[81].

745

746 Protein purification

747 Recombinant HAPLN2 was purified using the method to purify the versican core protein
748 G1 domain as previously described [82]. The HAPLN2 coding sequence, nucleotides 82–
749 1026 was amplified from mouse brain cDNA by PCR and cloned into pGEX6p-1
750 (Addgene, 27-4597-01). The glutathione-S-transferase tag was removed by PCR. The
751 construct was transformed into ClearColi® BL21(DE3) Electrocompetent Cells (LGC
752 Biosearch Technologies, 60810-1). The cells were grown in LB Miller broth containing
753 100 μg/mL ampicillin at 37ºC with shaking at 150 rpm. The *E. coli* cultures were induced
754 with 0.8 mM isopropyl β-D-thiogalactopyranoside (Nacalai Tesque, 06289-67), grown
755 for another 20 hours at 20ºC, and harvested by centrifugation at 10,000 × *g* for 20
756 minutes at 4ºC (Beckman Coulter, Avanti J-25). Inclusion bodies were purified and
757 solubilized in urea and the protein was refolded, essentially as described previously [82].
758 Briefly, inclusion bodies were isolated with an *E. coli* lysis buffer [1% (w/v) Nonidet P-
759 40, 1% (w/v) Triton X-100, 1 mM PMSF, and 1 mM DTT in PBS] solubilized in a
760 denaturation buffer [8 M urea in 50 mM Tris-HCl (pH 7.5)] and clarified by
761 centrifugation. The supernatant was purified by incubating with Ni-NTA agarose
762 (QIAGEN, 30210) overnight and eluted with elution buffer [6 M urea, 500 mM
763 imidazole, and 10 mM HCl] and then diluted 66-fold into refolding buffer [1 mM
764 ethylenediaminetetraacetic acid, 500 mM L-arginine, 1 mM cysteine, 2 mM cystine, and
765 20 mM ethanolamine (pH 11.0)] by dropwise addition at 4ºC with gentle stirring,
766 followed by incubation overnight without stirring. After refolding, the protein was
767 concentrated to 2 mL with Amicon Ultra-15 Centrifugal Filter 10 kDa MWCO

768 (Millipore, 36100101), and dialyzed overnight into a storage buffer [10 mM sodium
769 phosphate (pH 8.0)].

770

771 Protein aggregation assay

772 Recombinant HAPLN2 proteins (500 nM) were subjected to a series of pH (6.0–8.0),
773 NaCl concentration (0–300 mM), and hyaluronic acid (0–1 mg/mL) in a total volume of
774 100 μL. The samples were deposited on μ-Slide 18-Well Glass Bottom (Ibidi, 81817) and
775 incubated for 24 hours at 37ºC before being imaged on Eclipse Ti2 microscope (Nikon
776 Corporation) with Micromanager software [83] in which bright field images were taken
777 using a 20X air magnification objective. Aggregate formation was imaged by collecting a
778 series of images in the bright field channel. Fiji software was used in all image
779 processing.

780

781 *In vitro* single-aggregate imaging

782 Super-resolution imaging was conducted based on point accumulation for imaging
783 nanoscale topography (PAINT). Borosilicate glass coverslips (VWR International, 22 ×
784 22 mm, 631-0124) were cleaned with an argon plasma cleaner (Harrick Plasma, PDC-
785 002) for at least one hour to remove fluorescent residues. Before use, each batch of cover
786 slides was tested for fluorescent artifacts. A drop of 10 μL of the mixture of HAPLN2
787 used in the protein aggregation assay was placed over a coverslip together with
788 Thioflavin T and Nile Red dyes diluted in PBS to achieve final concentrations of 5 μM
789 for Thioflavin T and 5 nM for Nile Red. Imaging was performed using a CFI
790 Apochromat TIRF 100x Oil immersion objective (Nikon Corporation), mounted on an
791 Eclipse Ti2 microscope (Nikon Corporation). Thioflavin T was excited using a 405 nm
792 laser (Cobolt #0405-06-01-0120-100) with a beam power of 20 mW. Emitted
793 fluorescence was collected by the same objective and separated from the excitation light
794 by a dichroic (Semrock #DI03-R405/488/532/635-T1-25X36), subsequently passed

through an emission filter (Semrock #FF01-510/84-25) and focused onto a CMOS camera (ORCA-Flash4.0 V3 Digital CMOS; Hamamatsu). Nile Red was excited by a 532nm laser (Cobolt #0532-06-91-0100-100) with a beam power of 80 mW. Both lasers were positioned at a highly inclined and laminated optical sheet (HiLo) illumination angle to image large amorphous aggregates at the surface of the coverslip (exciting ~5 µm deep in the sample) while minimizing background fluorescence. Emitted light was separated using a dichroic (DC/ZT532rdc-UF2; Chroma) and passed through an emission filter (Semrock #FF01-650/150-25) before being focused onto the CMOS camera. The image pixel size was 65 nm. A z-stack of 5.0 µm (10 planes with 0.5 µm spacing) was acquired in all channels. The microscope was controlled with Micromanager software, and the frame interval was 50 ms. Each analyzed image corresponds to an average of 10 images in the bright-field channel, 50 images in the thioflavin T, and 1,000 images in the Nile Red channel. The Nile Red images were reconstructed with the ThunderSTORM plug-in in Fiji software [84]. The morphological analysis of Nile Red-positive structures from reconstructed images was conducted by LocAlization Microscopy Analyzer (LAMA) [52] and MATLAB (Mathworks, ver. R2023b).

Negative-stained transmission electron microscopy

1.5 µL of recombinant samples were deposited onto glow-discharged formvar-coated 300-mesh copper grids (Stork Veco, Eerbeek, The Netherlands) for 20 minutes at room temperature. The grids were blotted with filter paper (Toyo Roshi Kaisha, Ltd., Tokyo, Japan), washed twice with PBS, washed twice with distilled water, stained with 2% (w/v) uranyl acetate for 30 seconds, blotted and air-dried. The prepared specimens were finally examined with an electron microscope (HT7700; Hitachi, Tokyo, Japan) at 100 kV.

Stereotaxic injection

821 Mice were anesthetized by intraperitoneal injection with 5.0 mL/kg of a non-narcotic
822 anesthetic combination (Me/Mi/Bu) [30 µg/mL medetomidine (Zenoaq), 0.4 mg/mL
823 midazolam (Astellas), and 0.5 mg/mL butorphanol (Meiji Seika Pharma)] and fixed in a
824 stereotaxic surgery frame.

825 For intracerebellar injection, 20 mg/mL hyaluronidase from ovine testes (FUJIFILM
826 Wako Pure Chemical Corporation, 37326-33-3) in a total volume of 1.0 µL was injected
827 at the following coordinates relative to the bregma: anterior-posterior (A/P) -5.5 mm
828 medial-lateral (M/L) -1.2 mm, and dorsal-ventral (D/V) -2.5 mm. Mice were sacrificed
829 one day post-surgery.

830 For intrahippocampal injection, either 15 pmol of protein or 5 mg/mL LPS solution, each
831 in a total volume of 2.0 µL, was injected at the following coordinates relative to the
832 bregma: A/P -1.7 mm, M/L -1.6 mm, and D/V -1.9 mm. Mice were sacrificed one week
833 post-surgery.

834

835 Depletion of microglia by PLX3397 treatment

836 PLX3397 [85] was synthesized as described previously [86] and formulated at 290 mg/kg
837 in AIN-76A standard chow by Research Diets Inc. The chows were given to 4-week-old
838 wild-type mice (C57/BL6J) for two months. Depletion of microglia was confirmed by
839 immunohistochemistry for a microglial marker Iba1.

840

841 RNA isolation and quantitative real-time PCR

842 Total RNA was extracted from MG6 cells grown in 12-well tissue culture plates (7×10^4
843 cells/well) by High Pure RNA Isolation Kit (Roche, 11828665001). The isolated total
844 RNA was then reverse-transcribed with ReverTra Ace (TOYOBO, FSQ-201). cDNAs
845 were amplified with THUNDERBIRD Probe qPCR mix (Toyobo, QPS-101), and

846 Universal Probe Library probe (Roche) the following specific primer sets. mRNA levels
847 were measured with LightCycler® 480 (Roche).

Gene	Forward (5'–3')	Reverse (5'–3')
Il6	TGTGAAATCAGGATGCTCTGG	CACTTTATTGGGCTCTATACAATATGC
Tnf	TCTTCTCATTCCTGCTTGTGG	GGTCTGGGCCATAGAACTGA
Actb	ACCAGAGGCATACAGGGACA	CTAAGGCCAACCGTGAAAAG

848

849 # Statistics and reproducibility

850 All data were derived from at least three independent experiments and are presented as
851 mean ± S.D. unless otherwise stated in the figure legends. Statistical analyses were
852 performed with GraphPad Prism 9.0 software. An unpaired two-tailed Student's *t*-test or
853 one-way ANOVA followed by Tukey's *post hoc* test was performed as described in the
854 figure legends. All replication attempts were successful with similar results.

855

856 # Acknowledgments

857 We thank members of the Laboratory of Morphology and Image Analysis, Biomedical
858 Research Core Facilities, and Juntendo University Graduate School of Medicine for
859 technical assistance with microscopy.

860

861 # Author Contributions

862 A.W. did most of the experimental work *in vivo* and *in vitro*, designed the experiments,
863 analyzed data, and wrote the paper. S.H. conceived the project, designed the experiments,
864 performed fractionation experiments, MS analysis, stereotaxic injection, and
865 immunohistochemical analysis of HAPLN2, analyzed data, and wrote the paper. K.I.

performed fractionation experiments, stereotaxic injection, and immunohistochemical analysis of HAPLN2, and analyzed data. S. Marchese, P. E., and V.M. provided technical support for HiLo imaging and analyzed data. H.K. performed EM analysis, analyzed data, and wrote the paper. S.T. provided technical support for stereotaxic injection, discussed the results, and analyzed data. M.K. provided technical support for EM analysis, designed the experiments, and analyzed data. T.S. and M.T. provided post-mortem human brains. J.A.V. provided technical support for HiLo imaging, analyzed data, discussed the results, and wrote the paper. T.T. provided technical support for stereotaxic injection and analyzed data. S. Murata conceived the project, designed the experiments, analyzed data, and wrote the paper. All authors reviewed the final version and agreed to its publication.

References

[1] Chung CG, Lee H, Lee SB. Mechanisms of protein toxicity in neurodegenerative diseases. *Cellular and Molecular Life Sciences* 2018; 75: 3159–3180.

[2] Chou A-H, Yeh T-H, Ouyang P, et al. Polyglutamine-expanded ataxin-3 causes cerebellar dysfunction of SCA3 transgenic mice by inducing transcriptional dysregulation. *Neurobiol Dis* 2008; 31: 89–101.

[3] Lustbader JW, Cirilli M, Lin C, et al. ABAD Directly Links Aβ to Mitochondrial Toxicity in Alzheimer's Disease. *Science (1979)* 2004; 304: 448–452.

[4] Kastelic M, Kalyuzhnyi Y V., Hribar-Lee B, et al. Protein aggregation in salt solutions. *Proceedings of the National Academy of Sciences* 2015; 112: 6766–6770.

[5] Cui Q, Liu Z, Bai G. Friend or foe: The role of stress granule in neurodegenerative disease. *Neuron* 2024; 112: 2464–2485.

[6] Bachiller S, Jiménez-Ferrer I, Paulus A, et al. Microglia in Neurological Diseases: A Road Map to Brain-Disease Dependent-Inflammatory Response. *Front Cell Neurosci* 2018; 12: 488.

[7] Kelmer Sacramento E, Kirkpatrick JM, Mazzetto M, et al. Reduced proteasome activity in the aging brain results in ribosome stoichiometry loss and aggregation. *Mol Syst Biol* 2020; 16: e9596.

[8] Shibata M, Lu T, Furuya T, et al. Regulation of intracellular accumulation of mutant huntingtin by beclin 1. *Journal of Biological Chemistry* 2006; 281: 14474–14485.

[9] Lipinski MM, Zheng B, Lu T, et al. Genome-wide analysis reveals mechanisms modulating autophagy in normal brain aging and in Alzheimer's disease. *Proceedings of the National Academy of Sciences* 2010; 107: 14164–14169.

[10] Pan J, Ma N, Yu B, et al. Transcriptomic profiling of microglia and astrocytes throughout aging. *J Neuroinflammation* 2020; 17: 97.

900 [11] Pluvinage J V., Haney MS, Smith BAH, et al. CD22 blockade restores homeostatic microglial
901 phagocytosis in ageing brains. *Nature* 2019; 568: 187–192.

902 [12] Da Mesquita S, Herz J, Wall M, et al. Aging-associated deficit in CCR7 is linked to worsened
903 glymphatic function, cognition, neuroinflammation, and β-amyloid pathology. *Sci Adv* 2021; 7:
904 4601–4622.

905 [13] Vilchez D, Saez I, Dillin A. The role of protein clearance mechanisms in organismal ageing and
906 age-related diseases. *Nat Commun* 2014; 5: 5659.

907 [14] Safaiyan S, Kannaiyan N, Snaidero N, et al. Age-related myelin degradation burdens the clearance
908 function of microglia during aging. *Nat Neurosci* 2016; 19: 995–998.

909 [15] Crystal H, Dickson D, Fuld P, et al. Clinico-pathologic studies in dementia: nondemented subjects
910 with pathologically confirmed Alzheimer's disease. *Neurology* 1988; 38: 1682–1687.

911 [16] Iseki E, Tsunoda S, Suzuki K, et al. Regional quantitative analysis of NFT in brains of
912 non-demented elderly persons: Comparisons with findings in brains of late-onset Alzheimer's
913 disease and limbic NFT dementia. *Neuropathology* 2002; 22: 34–39.

914 [17] Schweighauser M, Arseni D, Bacioglu M, et al. Age-dependent formation of TMEM106B amyloid
915 filaments in human brains. *Nature* 2022; 605: 310–314.

916 [18] Kenyon C, Chang J, Gensch E, et al. A C. elegans mutant that lives twice as long as wild type.
917 *Nature* 1993; 366: 461–464.

918 [19] Lin K, Dorman JB, Rodan A, et al. daf-16 : An HNF-3/forkhead Family Member That Can
919 Function to Double the Life-Span of Caenorhabditis elegans. *Science (1979)* 1997; 278: 1319–
920 1322.

921 [20] Hsu A-L, Murphy CT, Kenyon C. Regulation of Aging and Age-Related Disease by DAF-16 and
922 Heat-Shock Factor. *Science (1979)* 2003; 300: 1142–1145.

923 [21] Morley JF, Morimoto RI. Regulation of Longevity in Caenorhabditis elegans by Heat Shock Factor
924 and Molecular Chaperones. *Mol Biol Cell* 2004; 15: 657–664.

925 [22] David DC, Ollikainen N, Trinidad JC, et al. Widespread Protein Aggregation as an Inherent Part of
926 Aging in C. elegans. *PLoS Biol* 2010; 8: e1000450.

927 [23] Walther DM, Kasturi P, Zheng M, et al. Widespread proteome remodeling and aggregation in aging
928 C. elegans. *Cell* 2015; 161: 919–932.

929 [24] Fares H, Greenwald I. Genetic Analysis of Endocytosis in Caenorhabditis elegans : Coelomocyte
930 Uptake Defective Mutants. *Genetics* 2001; 159: 133–145.

931 [25] Gallotta I, Sandhu A, Peters M, et al. Extracellular proteostasis prevents aggregation during
932 pathogenic attack. *Nature* 2020; 584: 410–414.

933 [26] Diner I, Hales CM, Bishof I, et al. Aggregation Properties of the Small Nuclear Ribonucleoprotein
934 U1-70K in Alzheimer Disease. *Journal of Biological Chemistry* 2014; 289: 35296–35313.

935 [27] Hales CM, Dammer EB, Deng Q, et al. Changes in the detergent-insoluble brain proteome linked to
936 amyloid and tau in Alzheimer's Disease progression. *Proteomics* 2016; 16: 3042–3053.

937 [28] Guo Q, Dammer EB, Zhou M, et al. Targeted Quantification of Detergent-Insoluble RNA-Binding
938 Proteins in Human Brain Reveals Stage and Disease Specific Co-aggregation in Alzheimer's
939 Disease. *Front Mol Neurosci* 2021; 14: 623659.

940 [29] Woltjer RL, Cimino PJ, Boutté AM, et al. Proteomic determination of widespread detergent
941 insolubility, including Aβ but not tau, early in the pathogenesis of Alzheimer's disease. *The FASEB*
942 *Journal* 2005; 19: 1923–1925.

943 [30] Diner I, Nguyen T, Seyfried NT. Enrichment of Detergent-insoluble Protein Aggregates from
944 Human Postmortem Brain. *J Vis Exp* 2017; 2017: 55835.

945 [31] Gozal YM, Duong DM, Gearing M, et al. Proteomics Analysis Reveals Novel Components in the
946 Detergent-Insoluble Subproteome in Alzheimer's Disease. *J Proteome Res* 2009; 8: 5069–5079.

947 [32] Mawuenyega KG, Sigurdson W, Ovod V, et al. Decreased Clearance of CNS β-Amyloid in
948 Alzheimer's Disease. *Science (1979)* 2010; 330: 1774–1774.

949 [33] Hier DB, Azizi S, Thimgan MS, et al. Tau kinetics in Alzheimer's disease. *Front Aging Neurosci*
950 2022; 14: 1055170.

951 [34] Masuda T, Tomita M, Ishihama Y. Phase transfer surfactant-aided trypsin digestion for membrane
952 proteome analysis. *J Proteome Res* 2008; 7: 731–740.

953 [35] Cuanalo-Contreras K, Schulz J, Mukherjee A, et al. Extensive accumulation of misfolded protein
954 aggregates during natural aging and senescence. *Front Aging Neurosci* 2023; 14: 1090109.

955 [36] Chang E, Kuret J. Detection and quantification of tau aggregation using a membrane filter assay.
956 *Anal Biochem* 2008; 373: 330–336.

957 [37] Xu G, Gonzales V, Borchelt DR. Rapid Detection of Protein Aggregates in the Brains of Alzheimer
958 Patients and Transgenic Mouse Models of Amyloidosis. *Alzheimer Dis Assoc Disord* 2002; 16:
959 191–195.

960 [38] Sugitani K, Egorova D, Mizumoto S, et al. Hyaluronan degradation and release of a hyaluronan-
961 aggrecan complex from perineuronal nets in the aged mouse brain. *Biochim Biophys Acta Gen Subj*
962 2021; 1865: 129804.

963 [39] Bekku Y, Vargová L, Goto Y, et al. Bral1: Its Role in Diffusion Barrier Formation and Conduction
964 Velocity in the CNS. *The Journal of Neuroscience* 2010; 30: 3113–3123.

965 [40] Ximerakis M, Lipnick SL, Innes BT, et al. Single-cell transcriptomic profiling of the aging mouse
966 brain. *Nat Neurosci* 2019; 22: 1696–1708.

967 [41] Elbaz B, Darwish A, Vardy M, et al. The bone transcription factor Osterix controls extracellular
968 matrix- and node of Ranvier-related gene expression in oligodendrocytes. *Neuron* 2024; 112: 247-
969 263.e6.

970 [42] Grundke-Iqbal I, Iqbal K, Quinlan M, et al. Microtubule-associated protein tau. A component of
971 Alzheimer paired helical filaments. *Journal of Biological Chemistry* 1986; 261: 6084–6089.

972 [43] Fawcett JW, Oohashi T, Pizzorusso T. The roles of perineuronal nets and the perinodal
973 extracellular matrix in neuronal function. *Nat Rev Neurosci* 2019; 20: 451–465.

974 [44] Dohm-Hansen S, English JA, Lavelle A, et al. The 'middle-aging' brain. *Trends Neurosci* 2024; 47:
975 259–272.

976 [45] Babinchak WM, Haider R, Dumm BK, et al. The role of liquid–liquid phase separation in
977 aggregation of the TDP-43 low-complexity domain. *Journal of Biological Chemistry* 2019; 294:
978 6306–6317.

979 [46] Qamar S, Wang G, Randle SJ, et al. FUS Phase Separation Is Modulated by a Molecular Chaperone
980 and Methylation of Arginine Cation-π Interactions. *Cell* 2018; 173: 720-734.e15.

981 [47] Maharana S, Wang J, Papadopoulos DK, et al. RNA buffers the phase separation behavior of prion-
982 like RNA binding proteins. *Science (1979)* 2018; 360: 918–921.

983 [48] Patel A, Lee HO, Jawerth L, et al. A Liquid-to-Solid Phase Transition of the ALS Protein FUS
984 Accelerated by Disease Mutation. *Cell* 2015; 162: 1066–1077.

985 [49] Van Lindt J, Bratek-Skicki A, Nguyen PN, et al. A generic approach to study the kinetics of liquid–
986 liquid phase separation under near-native conditions. *Commun Biol* 2021; 4: 77.

987 [50] Danial JSH, Klenerman D. Single molecule imaging of protein aggregation in Dementia: Methods,
988 insights and prospects. *Neurobiol Dis* 2021; 153: 105327.

989 [51] Lim D, Chu KK, Mertz J. Wide-field fluorescence sectioning with hybrid speckle and uniform-
990 illumination microscopy. *Opt Lett* 2008; 33: 1819.

991 [52] Malkusch S, Heilemann M. Extracting quantitative information from single-molecule super-
992 resolution imaging data with LAMA – LocAlization Microscopy Analyzer. *Sci Rep* 2016; 6: 34486.

993 [53] Bondareff W, Narotzky R. Age Changes in the Neuronal Microenvironment. *Science (1979)* 1972;
994 176: 1135–1136.

995 [54] Syková E, Vořišek I, Antonova T, et al. Changes in extracellular space size and geometry in APP23
996 transgenic mice: A model of Alzheimer's disease. *Proceedings of the National Academy of*
997 *Sciences* 2005; 102: 479–484.

998 [55] Reed MJ, Vernon RB, Damodarasamy M, et al. Microvasculature of the Mouse Cerebral Cortex
999 Exhibits Increased Accumulation and Synthesis of Hyaluronan With Aging. *J Gerontol A Biol Sci*
1000 *Med Sci* 2017; 72: 740–746.

1001 [56] Cargill R, Kohama SG, Struve J, et al. Astrocytes in aged nonhuman primate brain gray matter
1002 synthesize excess hyaluronan. *Neurobiol Aging* 2012; 33: 830.e13-830.e24.

1003 [57] Reed MJ, Damodarasamy M, Pathan JL, et al. Increased Hyaluronan and TSG-6 in Association
1004 with Neuropathologic Changes of Alzheimer's Disease. *Journal of Alzheimer's Disease* 2019; 67:
1005 91–102.

1006 [58] Su W, Foster SC, Xing R, et al. CD44 Transmembrane Receptor and Hyaluronan Regulate Adult
1007 Hippocampal Neural Stem Cell Quiescence and Differentiation. *Journal of Biological Chemistry*
1008 2017; 292: 4434–4445.

1009 [59] Zakusilo FT, Kerry O'Banion M, Gelbard HA, et al. Matters of size: Roles of hyaluronan in CNS
1010 aging and disease. *Ageing Res Rev* 2021; 72: 101485.

1011 [60] Godin AG, Varela JA, Gao Z, et al. Single-nanotube tracking reveals the nanoscale organization of
1012 the extracellular space in the live brain. *Nature Nanotechnology 2016 12:3* 2016; 12: 238–243.

1013 [61] Wang WY, Tan MS, Yu JT, et al. Role of pro-inflammatory cytokines released from microglia in
1014 Alzheimer's disease. *Annals of Translational Medicine* 2015; 3: 136.

1015 [62] Elmore MRP, Najafi AR, Koike MA, et al. Colony-Stimulating Factor 1 Receptor Signaling Is
1016 Necessary for Microglia Viability, Unmasking a Microglia Progenitor Cell in the Adult Brain.
1017 *Neuron* 2014; 82: 380–397.

1018 [63] Subhramanyam CS, Wang C, Hu Q, et al. Microglia-mediated neuroinflammation in
1019 neurodegenerative diseases. *Semin Cell Dev Biol* 2019; 94: 112–120.

1020 [64] Molzahn C, Kuechler ER, Zemlyankina I, et al. Shift of the insoluble content of the proteome in the
1021 aging mouse brain. *Proc Natl Acad Sci U S A* 2023; 120: e2310057120.

1022 [65] Zolla V, Nizamutdinova IT, Scharf B, et al. Aging-related anatomical and biochemical changes in
1023 lymphatic collectors impair lymph transport, fluid homeostasis, and pathogen clearance. *Aging Cell*
1024 2015; 14: 582–594.

1025 [66] Tan Y-L, Yuan Y, Tian L. Microglial regional heterogeneity and its role in the brain. *Mol*
1026 *Psychiatry* 2020; 25: 351–367.

1027 [67] Savchenko VL, Nikonenko IR, Skibo GG. Microglial cells of the rat brain in postnatal period
1028 (comparative immunocytochemical analysis). *Neurophysiology* 1997; 29: 145–152.

1029 [68] Verdonk F, Roux P, Flamant P, et al. Phenotypic clustering: a novel method for microglial
1030 morphology analysis. *J Neuroinflammation* 2016; 13: 153.

1031 [69] Keller D, Erö C, Markram H. Cell Densities in the Mouse Brain: A Systematic Review. *Front*
1032 *Neuroanat*; 12. Epub ahead of print 23 October 2018. DOI: 10.3389/fnana.2018.00083.

1033 [70] Xie L, Kang H, Xu Q, et al. Sleep Drives Metabolite Clearance from the Adult Brain. *Science*
1034 *(1979)* 2013; 342: 373–377.

1035 [71] Decker Y, Németh E, Schomburg R, et al. Decreased pH in the aging brain and Alzheimer's
1036 disease. *Neurobiol Aging* 2021; 101: 40–49.

1037 [72] Crapser JD, Arreola MA, Tsourmas KI, et al. Microglia as hackers of the matrix: sculpting
1038 synapses and the extracellular space. *Cell Mol Immunol* 2021; 18: 2472–2488.

1039 [73] Tansley S, Gu N, Guzmán AU, et al. Microglia-mediated degradation of perineuronal nets
1040 promotes pain. *Science (1979)*. Epub ahead of print 26 May 2022. DOI:
1041 10.1126/SCIENCE.ABL6773.

1042 [74] Aires V, Coulon-Bainier C, Pavlovic A, et al. CD22 Blockage Restores Age-Related Impairments
1043 of Microglia Surveillance Capacity. *Front Immunol* 2021; 12: 43–57.

1044 [75] López-Otín C, Blasco MA, Partridge L, et al. Hallmarks of aging: An expanding universe. *Cell*
1045 2023; 186: 243–278.

1046 [76] Nakamichi K, Saiki M, Kitani H, et al. Suppressive effect of simvastatin on interferon-β-induced
1047 expression of CC chemokine ligand 5 in microglia. *Neurosci Lett* 2006; 407: 205–210.

1048 [77] Takenouchi T, Ogihara K, Sato M, et al. Inhibitory effects of U73122 and U73343 on Ca2+ influx
1049 and pore formation induced by the activation of P2X7 nucleotide receptors in mouse microglial cell
1050 line. *Biochim Biophys Acta* 2005; 1726: 177–186.

1051 [78] Sherman BT, Hao M, Qiu J, et al. DAVID: a web server for functional enrichment analysis and
1052 functional annotation of gene lists (2021 update). *Nucleic Acids Res* 2022; 50: W216–W221.

1053 [79] Iriki T, Iio H, Yasuda S, et al. Senescent cells form nuclear foci that contain the 26S proteasome.
1054 *Cell Rep* 2023; 42: 112880.

1055 [80] Schindelin J, Arganda-Carreras I, Frise E, et al. Fiji: an open-source platform for biological-image
1056 analysis. *Nature Methods 2012 9:7* 2012; 9: 676–682.

1057 [81] Bolte S, Cordelières FP. A guided tour into subcellular colocalization analysis in light microscopy.
1058 *J Microsc* 2006; 224: 213–32.

1059 [82] Clark SJ, Keenan TDL, Fielder HL, et al. Mapping the Differential Distribution of
1060 Glycosaminoglycans in the Adult Human Retina, Choroid, and Sclera. *Investigative Opthalmology*
1061 *& Visual Science* 2011; 52: 6511.

1062 [83] Edelstein AD, Tsuchida MA, Amodaj N, et al. Advanced methods of microscope control using
1063 μManager software. *J Biol Methods* 2014; 1: e10.

1064 [84] Ovesný M, Křížek P, Borkovec J, et al. ThunderSTORM: A comprehensive ImageJ plug-in for
1065 PALM and STORM data analysis and super-resolution imaging. *Bioinformatics* 2014; 30: 2389–
1066 2390.

1067 [85] Elmore MRP, Najafi AR, Koike MA, et al. Colony-stimulating factor 1 receptor signaling is
1068 necessary for microglia viability, unmasking a microglia progenitor cell in the adult brain. *Neuron*
1069 2014; 82: 380–397.

1070 [86] Tap WD, Wainberg ZA, Anthony SP, et al. Structure-Guided Blockade of CSF1R Kinase in
1071 Tenosynovial Giant-Cell Tumor. *New England Journal of Medicine* 2015; 373: 428–437.

1072 [87] Braak H, Alafuzoff I, Arzberger T, et al. Staging of Alzheimer disease-associated neurofibrillary
1073 pathology using paraffin sections and immunocytochemistry. *Acta Neuropathol* 2006; 112: 389–
1074 404.

1075 [88] Mirra SS, Heyman A, McKeel D, et al. The Consortium to Establish a Registry for Alzheimer's
1076 Disease (CERAD). *Neurology* 1991; 41: 479–486.

1077 [89] Thal DR, Rüb U, Orantes M, et al. Phases of Aβ-deposition in the human brain and its relevance for
1078 the development of AD. *Neurology* 2002; 58: 1791–1800.

1079 [90] McKeith IG, Boeve BF, Dickson DW, et al. Diagnosis and management of dementia with Lewy
1080 bodies. *Neurology* 2017; 89: 88–100.

1081 [91] Braak H, Tredici K Del, Rüb U, et al. Staging of brain pathology related to sporadic Parkinson's
1082 disease. *Neurobiol Aging* 2003; 24: 197–211.

1083 [92] Saito Y, Ruberu NN, Sawabe M, et al. Staging of Argyrophilic Grains: An Age-Associated
1084 Tauopathy. *J Neuropathol Exp Neurol* 2004; 63: 911–918.

1085 [93] Nelson PT, Dickson DW, Trojanowski JQ, et al. Limbic-predominant age-related TDP-43
1086 encephalopathy (LATE): consensus working group report. *Brain* 2019; 142: 1503–1527.

1087

1088 # Supporting information

1089 **S1 Fig. Protein Extraction by Phase Transfer Surfactant (PTS) Buffer.** Coomassie
1090 brilliant blue staining of young (3-month-old) and aged (28-month-old) mouse brains.
1091 Whole brains were lysed with PTS buffer and centrifuged at 15,000 × *g*.

1092 S2 Fig. Detailed Immunohistochemistry Analysis of HAPLN2 in Mouse Brains. (A)
1093 Magnified immunohistochemistry images of the mouse cerebellar white matter stained
1094 with anti-HAPLN2 antibody or biotinylated hyaluronic acid-binding protein (HABP),
1095 which probes hyaluronic acid. Specific staining of HAPLN2 and HABP was observed
1096 without crossover. (B, C) Fluorescence immunohistochemistry images of the mouse
1097 cerebellar white matter showing staining for ubiquitin (B) and p62 (C). Scale bars, 10
1098 μm.

1099 **S3 Fig. Aggregation Propensity of Recombinant HAPLN2 Protein.** (A, B) Brightfield
1100 microscopic images showing aggregates of recombinant HAPLN2 incubated under
1101 various buffer conditions in the absence (A) or presence (B) of hyaluronic acid. Scale
1102 bars represent 10 μm. (C) Histogram depicting the area of individual aggregates of
1103 recombinant HAPLN2 after 24 hours of incubation in the indicated buffer. Aggregate
1104 areas were measured using ImageJ (version 1.53t). (D) Transmission electron microscopy
1105 images of recombinant HAPLN2 aggregates formed under 150 mM NaCl (pH 6.0). Scale
1106 bars represent 1 μm (black) and 100 nm (white). (E) Schematic representation of cross-β-
1107 positive oligomers and fibrils stained with thioflavin T and Nile Red.

1108 **S4 Fig. Microglial Activation Induced by Injecting Recombinant HAPLN2 Protein**
1109 **into the Mouse Hippocampus.** (A) Filter trap assay and immunoblot analysis of
1110 recombinant full-length HAPLN2, HAPLN2 Ig-like domain, and oxStayGold proteins.
1111 These recombinant proteins (2 μM each) were incubated overnight at 37ºC, followed by
1112 centrifugation at 100,000 × *g* for one hour at 4ºC. (B) Immunohistochemistry images of
1113 the coronal brain section from Figure 8E, stained with anti-Iba1 antibody to probe
1114 activated microglia. Scale bar, 500 μm.

1115 **S1 Table. 31 proteins enriched in the sarkosyl-insoluble P2 fraction of aged mouse**
1116 **brains in Figure 1A.**

1117 **S2 Table. 45 proteins enriched in the PTS-soluble supernatant of aged mouse brains**
1118 **in Figure 1B.**

1119 **S3 Table. Human donors applied for the immunohistochemical analysis in Figure 9.**

1120 The stages of neurodegenerative diseases in post-mortem brain samples were examined
1121 using the following criteria. AT8: Tangle pathology (AT8 Stage)[87], CERAD: The
1122 Consortium to Establish a Registry for Alzheimer's Disease, assessing neuritic
1123 plaques[88], Thal: Amyloid-beta deposition (Thal Amyloid Phase)[89], DLB (4th
1124 Consensus): The Dementia with Lewy Bodies criteria (4th Consensus Report)[90], LB
1125 Braak: Lewy body pathology stages (Braak Staging for Lewy Bodies)[91], Grain:
1126 Argyrophilic grain pathology (Saito Scale)[92], Joseph-TDP: TDP-43 proteinopathy
1127 (Josephs' Staging)[93].

1128 **S4 Table. Primary Antibodies Used in Immunoblot and Immunohistochemistry**
1129 **Analyses.**

A

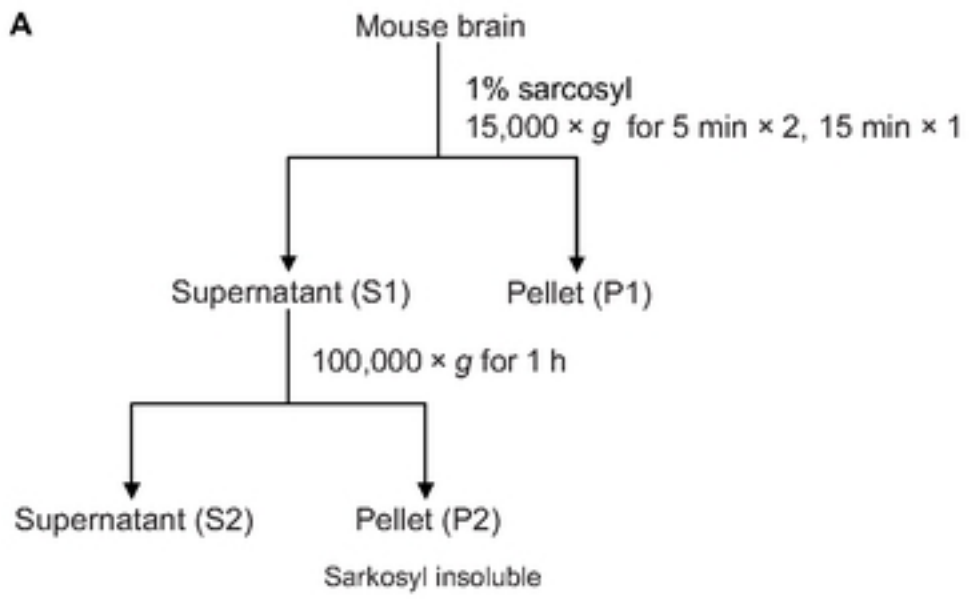

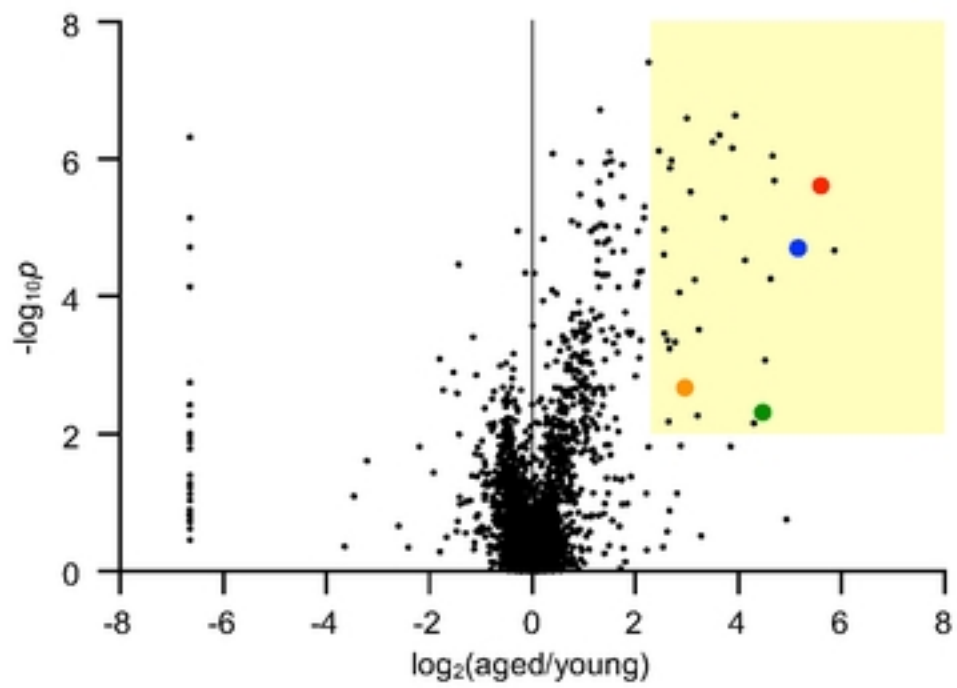

B

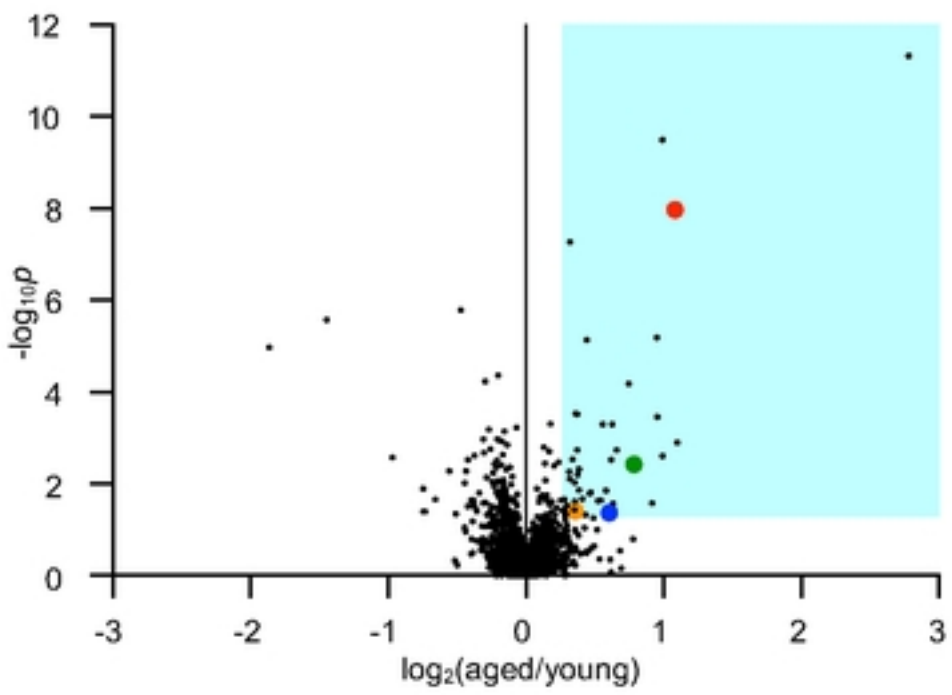

C

Protein	Fold change (aged)/(young)	
	Fig 1A	Fig 1B
Hyaluronan and proteoglycan link protein 2 (HAPLN2)	48.65	2.121
Immunoglobulin kappa constant (IGKC)	22.89	1.991
Bridging integrator 1 protein (BIN1)	6.384	1.990
Immunoglobulin mu chain C region (IGHM)	19.66	1.936
Aggrecan core protein (ACAN)	9.354	1.724
Claudin-11 (CLDN11)	13.19	1.550
Versican core protein (VCAN)	35.73	1.522
Hyaluronan and proteoglycan link protein 1 (HAPLN1)	7.786	1.284
Alpha-crystallin B chain (CRYAB)	8.017	1.247

D

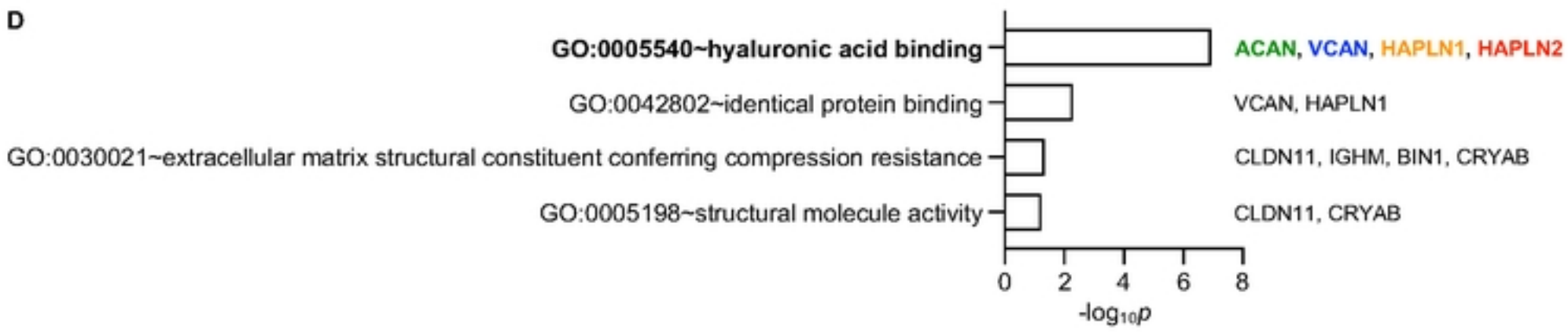

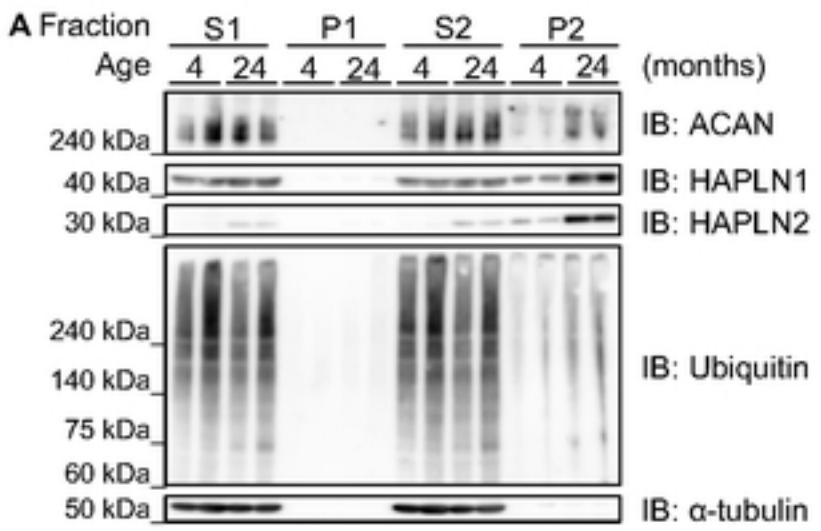
A
Fraction
S1
P1
S2
P2
Age
4 24 4 24 4 24 4 24
(months)
240 kDa
IB: ACAN
40 kDa
IB: HAPLN1
30 kDa
IB: HAPLN2
240 kDa
140 kDa
75 kDa
60 kDa
IB: Ubiquitin
50 kDa
IB: α-tubulin

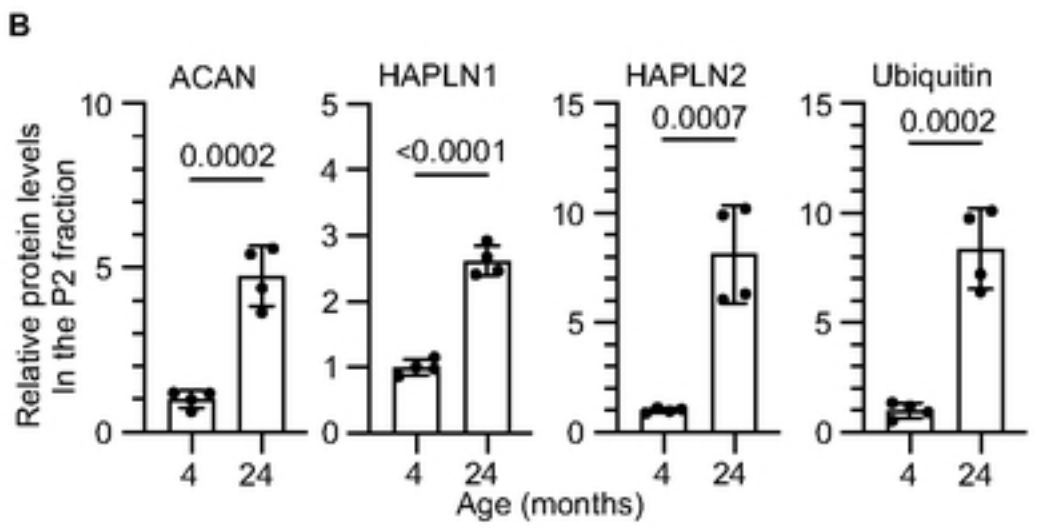
B
ACAN
HAPLN1
HAPLN2
Ubiquitin
0.0002
<0.0001
0.0007
0.0002
Relative protein levels
In the P2 fraction
Age (months)

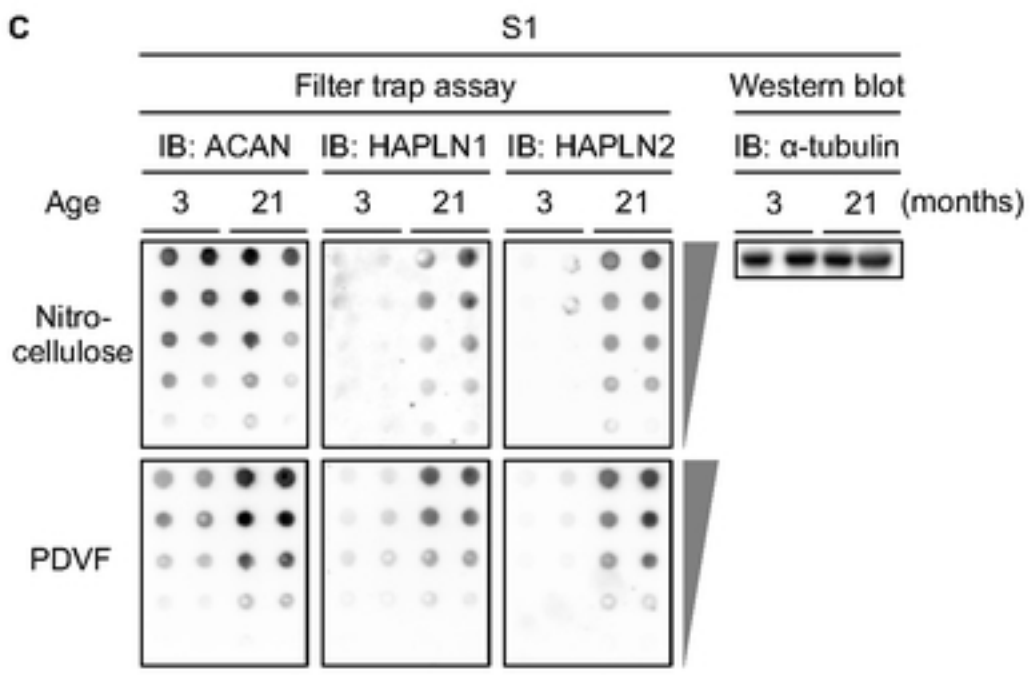
C
S1
Filter trap assay
Western blot
IB: ACAN
IB: HAPLN1
IB: HAPLN2
IB: α-tubulin
Age
3 21 3 21 3 21 3 21 (months)
Nitro-
cellulose
PDVF

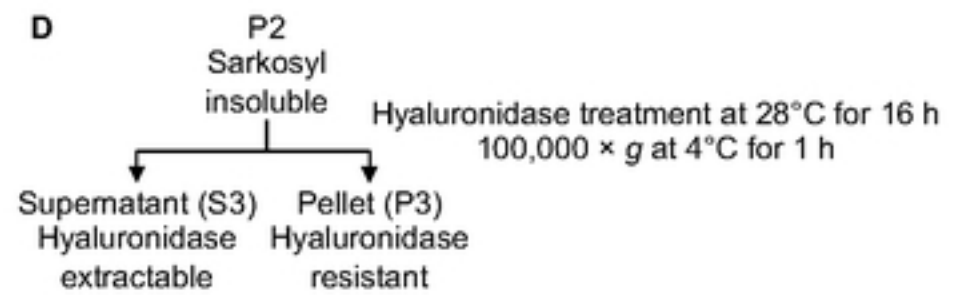
D
P2
Sarkosyl
insoluble
Hyaluronidase treatment at 28°C for 16 h
100,000 × g at 4°C for 1 h
Supernatant (S3)
Hyaluronidase
extractable
Pellet (P3)
Hyaluronidase
resistant

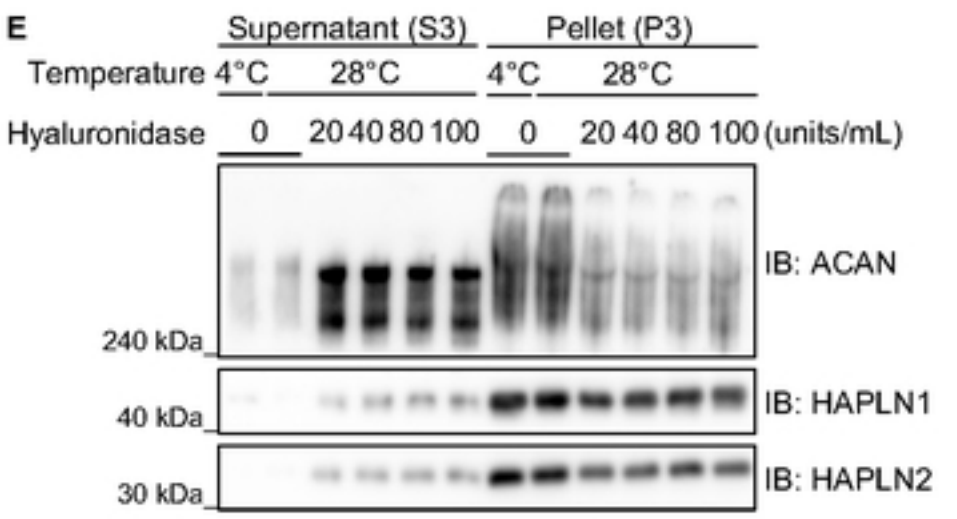
E
Supernatant (S3)
Pellet (P3)
Temperature
4°C
28°C
4°C
28°C
Hyaluronidase
0 20 40 80 100 0 20 40 80 100 (units/mL)
IB: ACAN
240 kDa
IB: HAPLN1
40 kDa
IB: HAPLN2
30 kDa

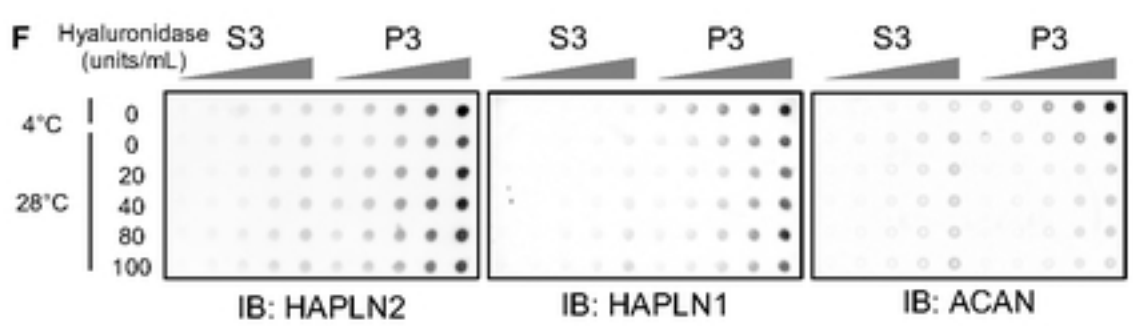
F
Hyaluronidase
(units/mL)
S3
P3
S3
P3
S3
P3
4°C
0
28°C
0
20
40
80
100
IB: HAPLN2
IB: HAPLN1
IB: ACAN

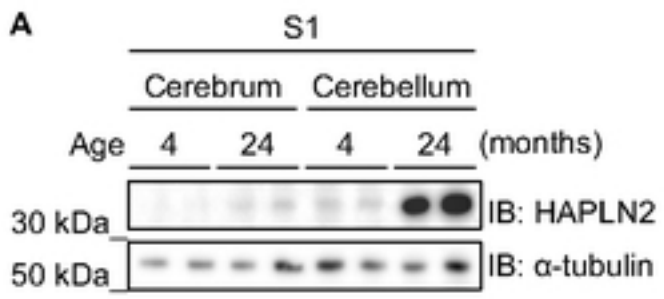
A
S1
Cerebrum
Cerebellum
Age 4 24 4 24 (months)
30 kDa
IB: HAPLN2
50 kDa
IB: α-tubulin

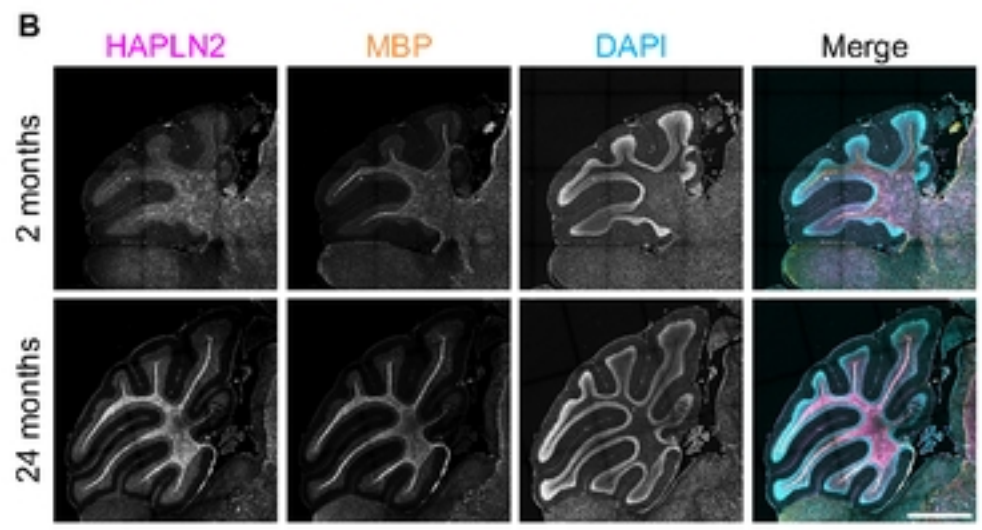
B
HAPLN2
MBP
DAPI
Merge
2 months
24 months

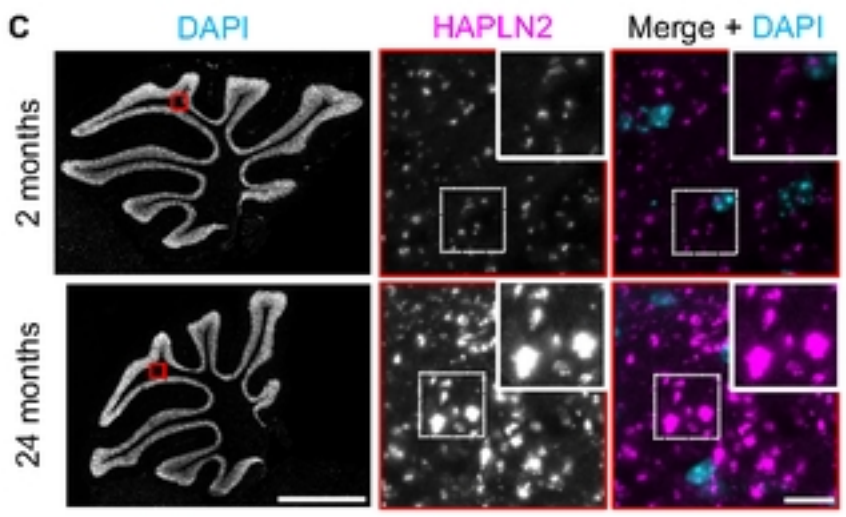
C
DAPI
HAPLN2
Merge + DAPI
2 months
24 months

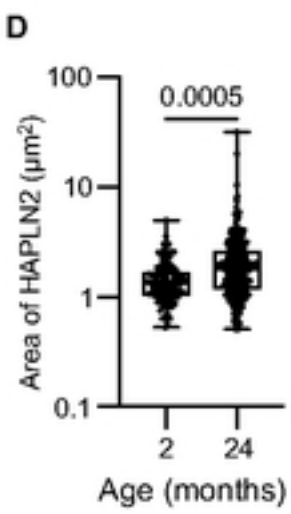
D
0.0005
Area of HAPLN2 (μm²)
100
10
1
0.1
2
24
Age (months)

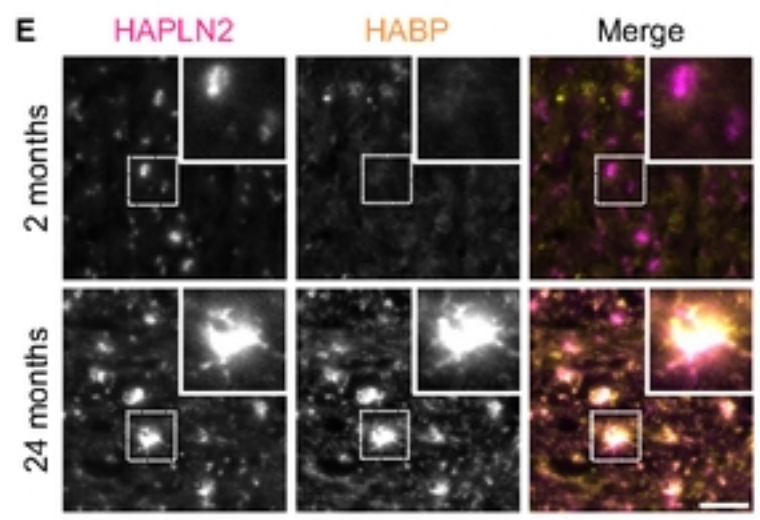
E
HAPLN2
HABP
Merge
2 months
24 months

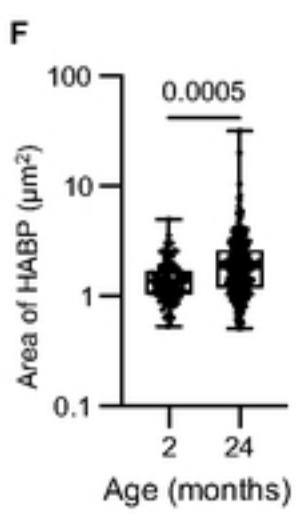
F
0.0005
Area of HABP (μm²)
100
10
1
0.1
2
24
Age (months)

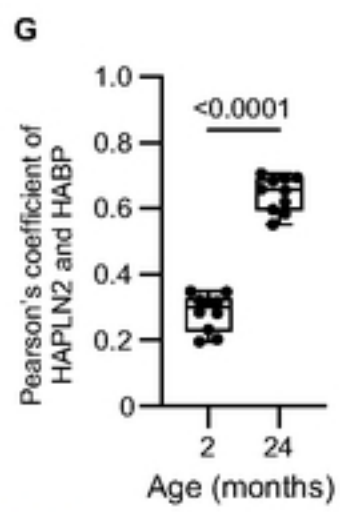
G
<0.0001
Pearson's coefficient of HAPLN2 and HABP
1.0
0.8
0.6
0.4
0.2
0
2
24
Age (months)

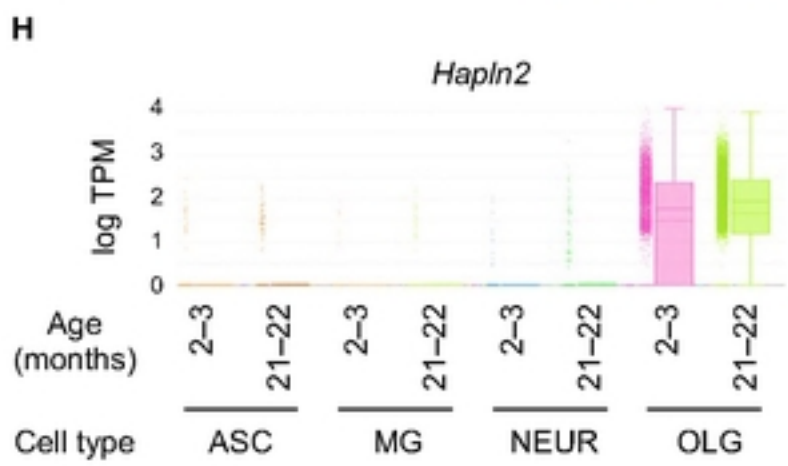
H
Hapln2
log TPM
4
3
2
1
0
Age (months)
2–3
21–22
Cell type
ASC
MG
NEUR
OLG

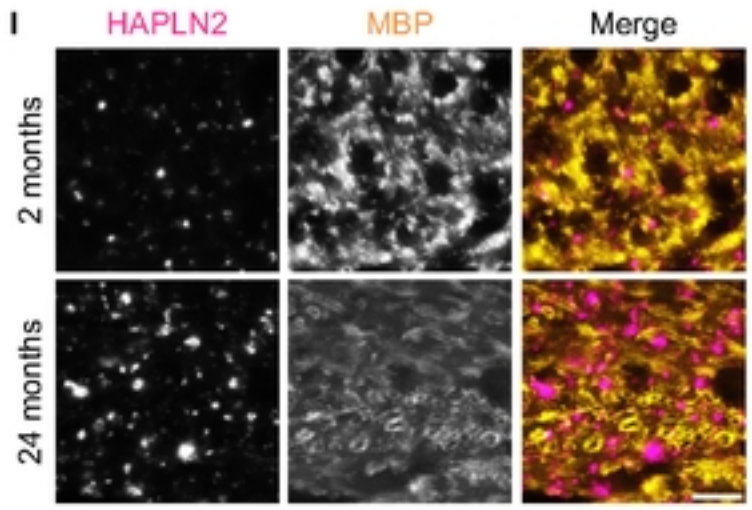
I
HAPLN2
MBP
Merge
2 months
24 months

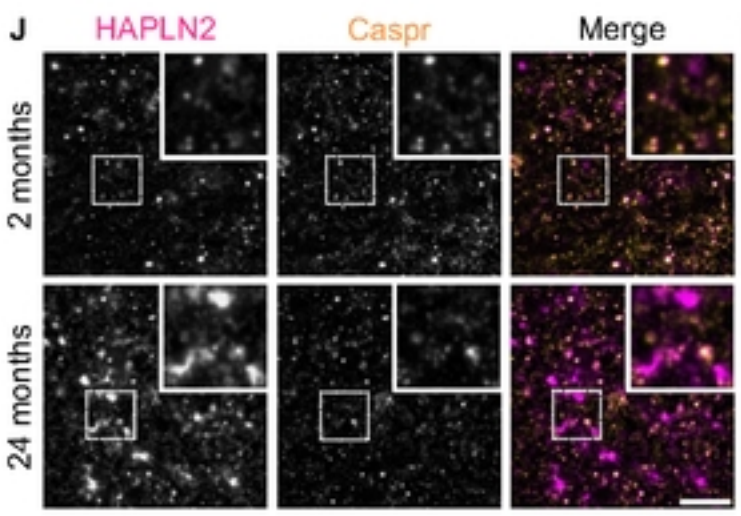
J
HAPLN2
Caspr
Merge
2 months
24 months

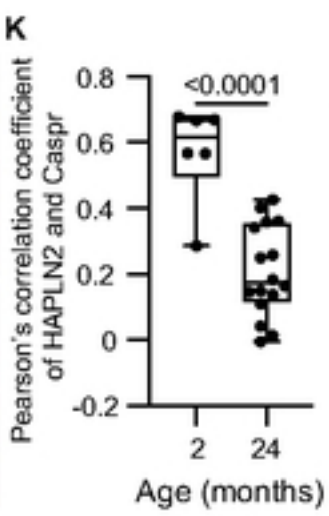
K
<0.0001
Pearson's correlation coefficient of HAPLN2 and Caspr
0.8
0.6
0.4
0.2
0
-0.2
2
24
Age (months)

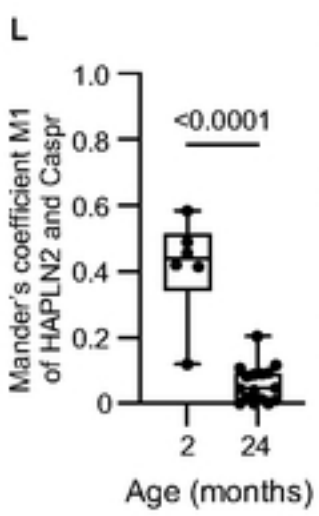
L
<0.0001
Mander's coefficient M1 of HAPLN2 and Caspr
1.0
0.8
0.6
0.4
0.2
0
2
24
Age (months)

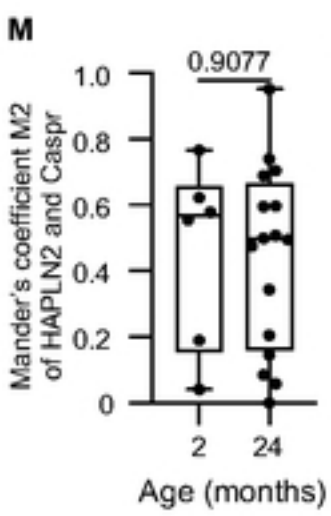
M
0.9077
Mander's coefficient M2 of HAPLN2 and Caspr
1.0
0.8
0.6
0.4
0.2
0
2
24
Age (months)

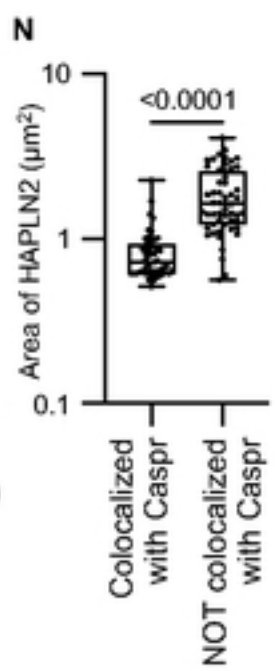
N
<0.0001
Area of HAPLN2 (μm²)
10
1
0.1
Colocalized with Caspr
NOT colocalized with Caspr

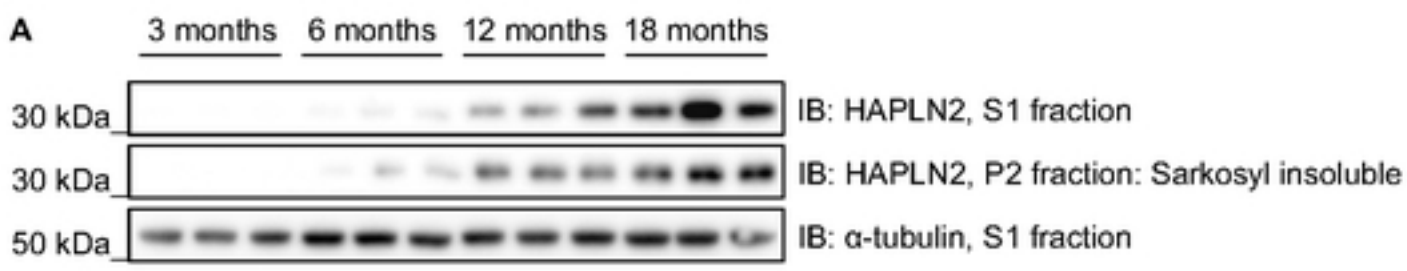
A
3 months
6 months
12 months
18 months
30 kDa
IB: HAPLN2, S1 fraction
30 kDa
IB: HAPLN2, P2 fraction: Sarkosyl insoluble
50 kDa
IB: α-tubulin, S1 fraction

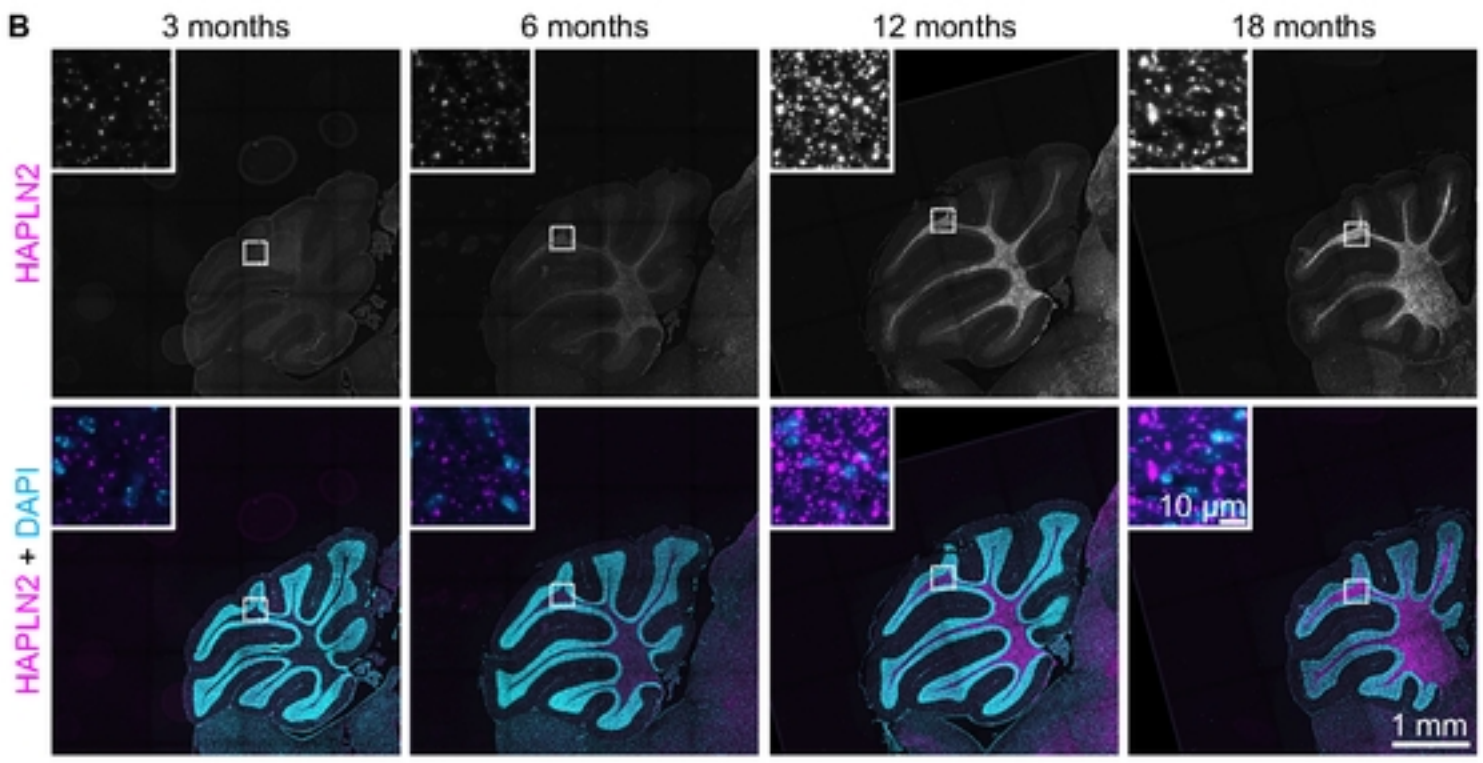
B
3 months
6 months
12 months
18 months
HAPLN2
HAPLN2 + DAPI
10 µm
1 mm

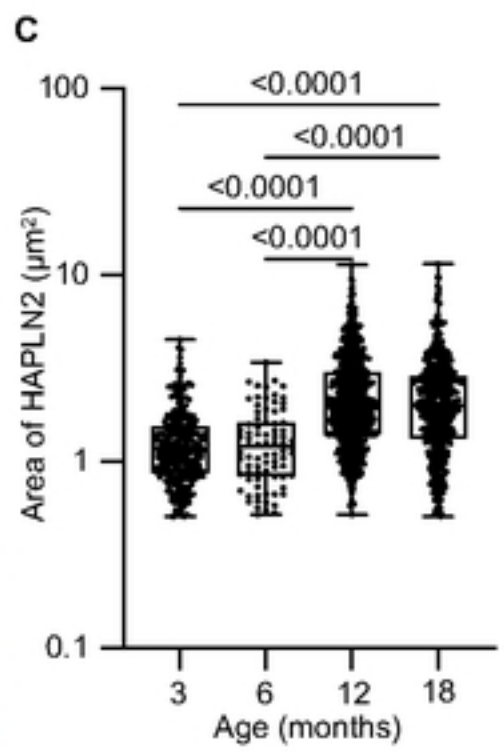
C
100
10
1
0.1
Area of HAPLN2 (µm²)
<0.0001
<0.0001
<0.0001
<0.0001
3
6
12
18
Age (months)

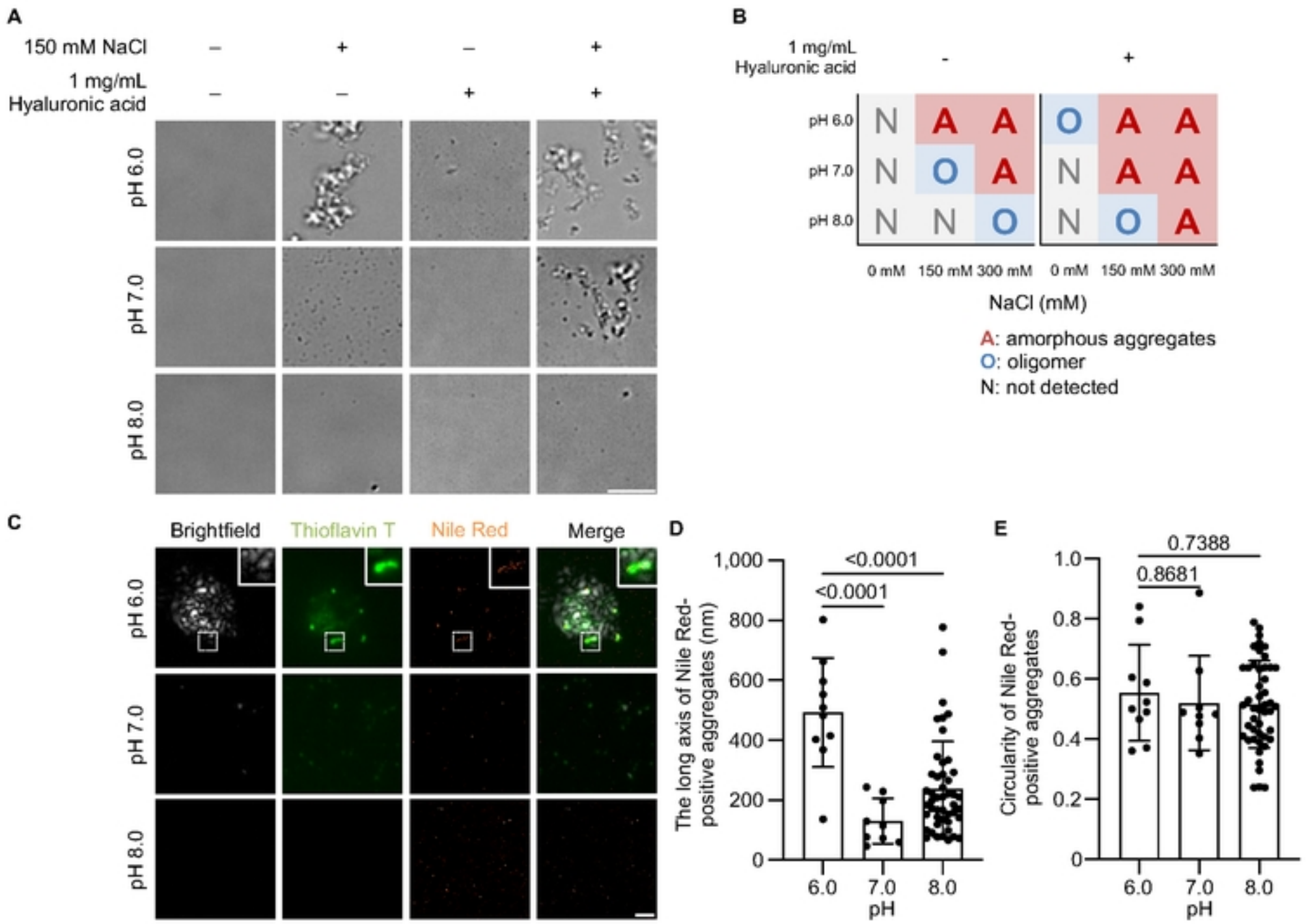
A
150 mM NaCl
1 mg/mL Hyaluronic acid
pH 6.0
pH 7.0
pH 8.0
B
1 mg/mL Hyaluronic acid
pH 6.0
pH 7.0
pH 8.0
0 mM 150 mM 300 mM 0 mM 150 mM 300 mM
NaCl (mM)
A: amorphous aggregates
O: oligomer
N: not detected
C
Brightfield
Thioflavin T
Nile Red
Merge
D
The long axis of Nile Red-positive aggregates (nm)
<0.0001
<0.0001
pH
E
Circularity of Nile Red-positive aggregates
0.7388
0.8681
pH

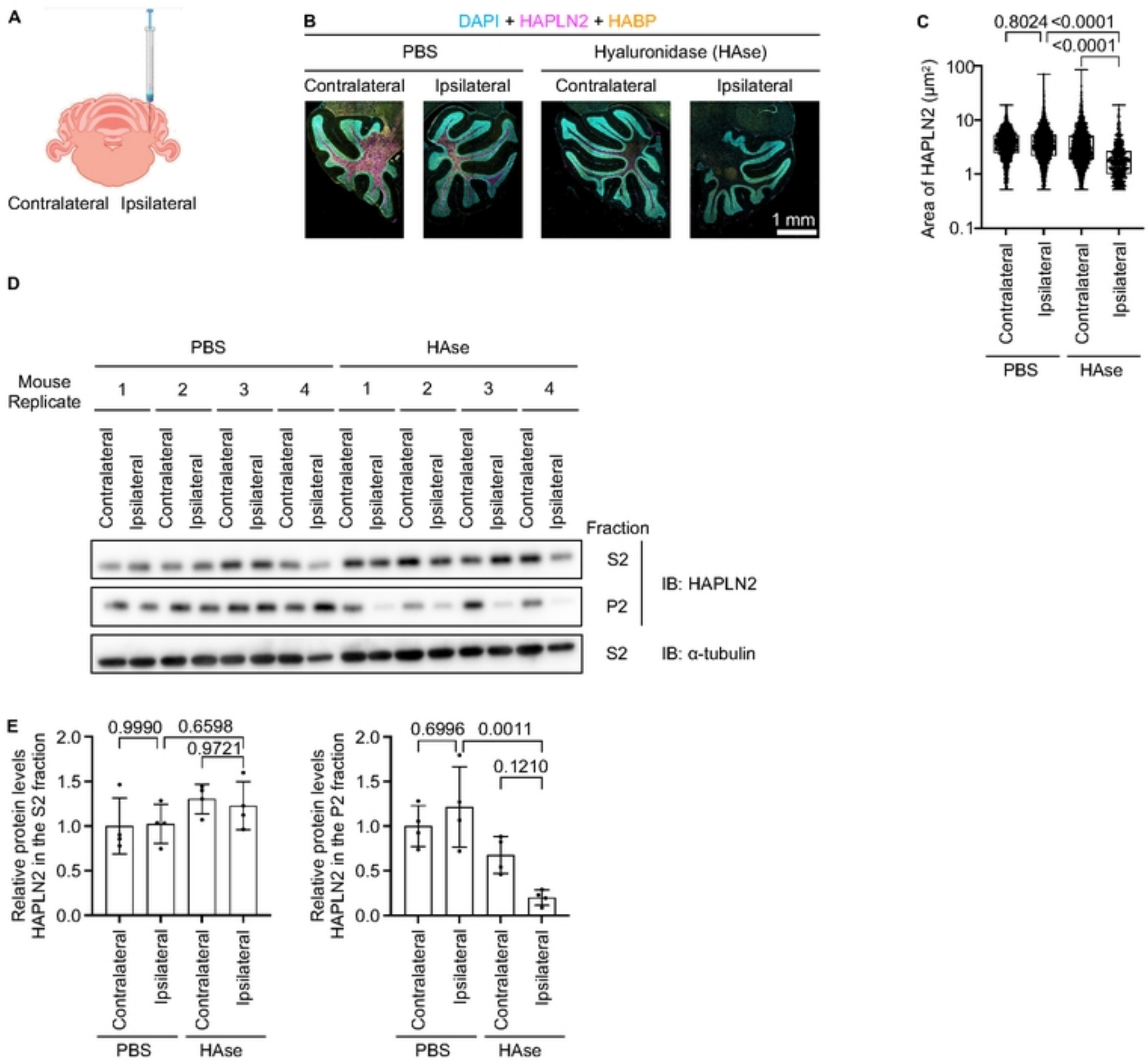
A
Contralateral
Ipsilateral
B
DAPI + HAPLN2 + HABP
PBS
Hyaluronidase (HAse)
Contralateral
Ipsilateral
Contralateral
Ipsilateral
1 mm
C
0.8024
<0.0001
<0.0001
Area of HAPLN2 (μm²)
100
10
1
0.1
Contralateral
Ipsilateral
Contralateral
Ipsilateral
PBS
HAse
D
PBS
HAse
Mouse Replicate
1
2
3
4
1
2
3
4
Contralateral
Ipsilateral
Fraction
S2
P2
IB: HAPLN2
S2
IB: α-tubulin
E
0.9990
0.6598
0.9721
Relative protein levels HAPLN2 in the S2 fraction
2.0
1.5
1.0
0.5
0.0
Contralateral
Ipsilateral
Contralateral
Ipsilateral
PBS
HAse
0.6996
0.0011
0.1210
Relative protein levels HAPLN2 in the P2 fraction
2.0
1.5
1.0
0.5
0.0
Contralateral
Ipsilateral
Contralateral
Ipsilateral
PBS
HAse

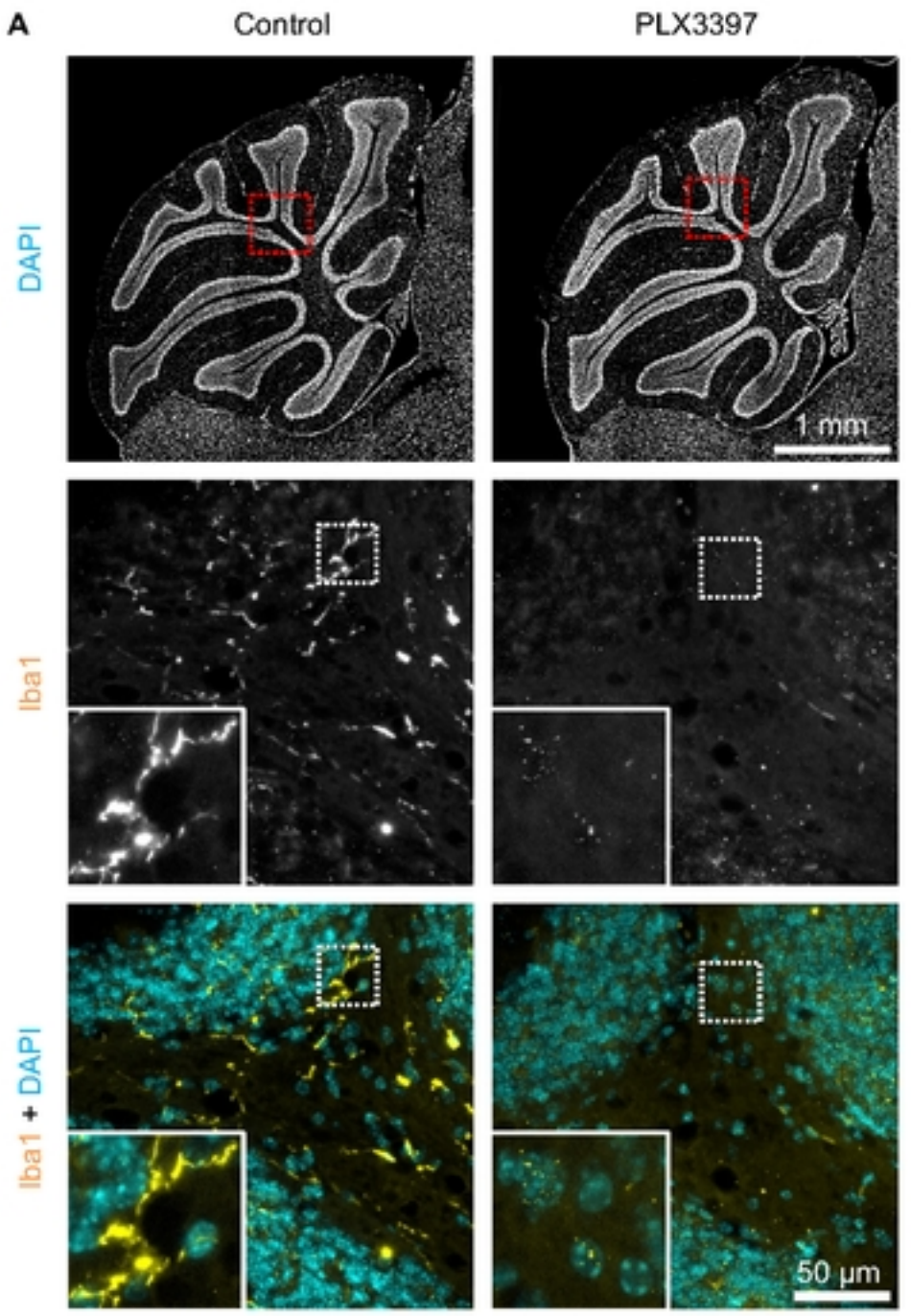
A
Control
PLX3397
DAPI
1 mm
Iba1
Iba1 + DAPI
50 µm

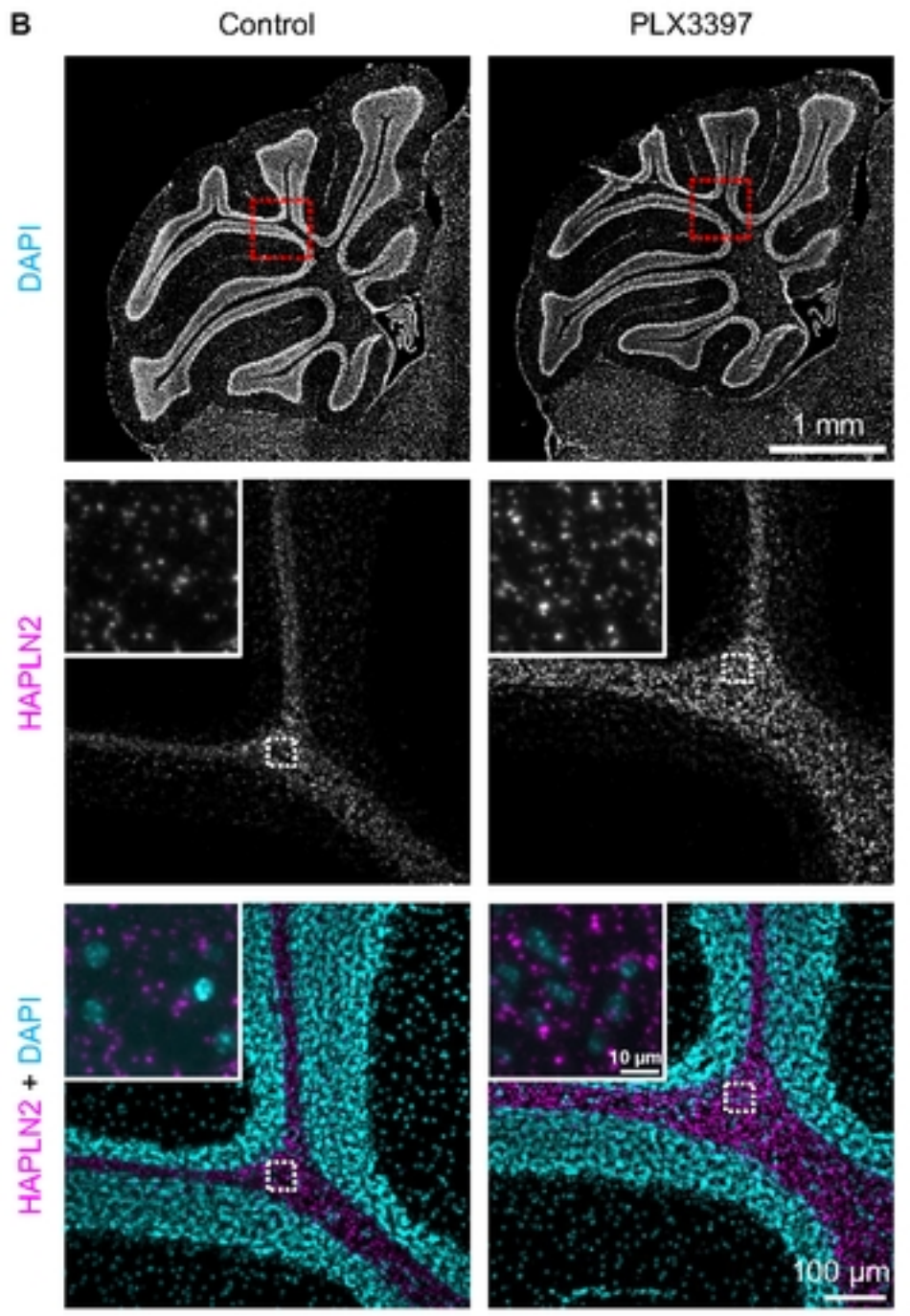
B
Control
PLX3397
DAPI
1 mm
HAPLN2
HAPLN2 + DAPI
10 µm
100 µm

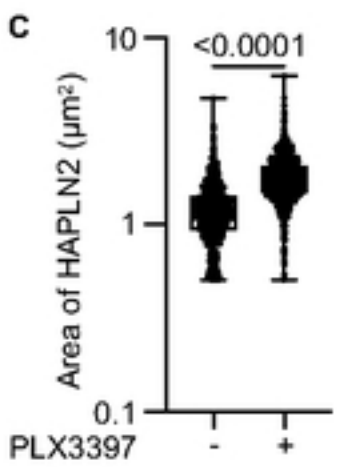
C
<0.0001
Area of HAPLN2 (µm²)
10
1
0.1
PLX3397
-
+

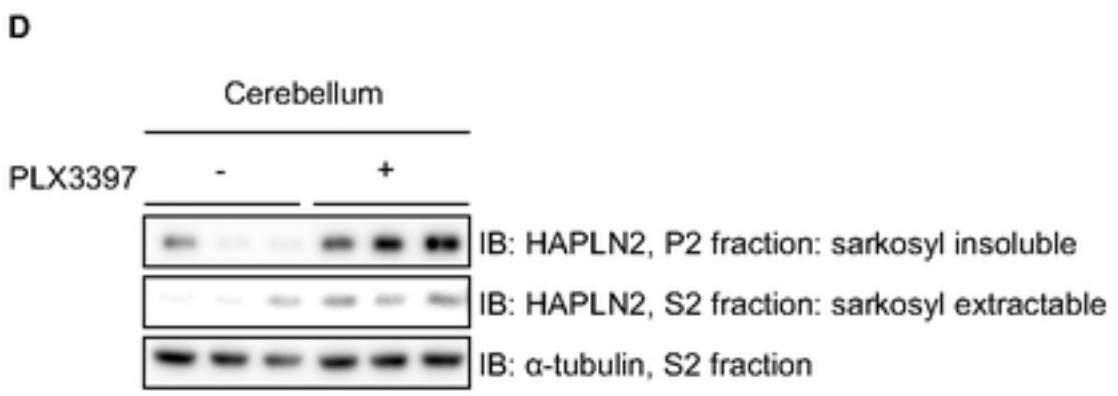
D
Cerebellum
PLX3397
-
+
IB: HAPLN2, P2 fraction: sarkosyl insoluble
IB: HAPLN2, S2 fraction: sarkosyl extractable
IB: α-tubulin, S2 fraction

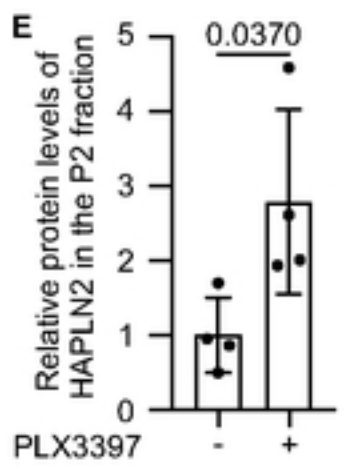
E
0.0370
Relative protein levels of HAPLN2 in the P2 fraction
5
4
3
2
1
0
PLX3397
-
+

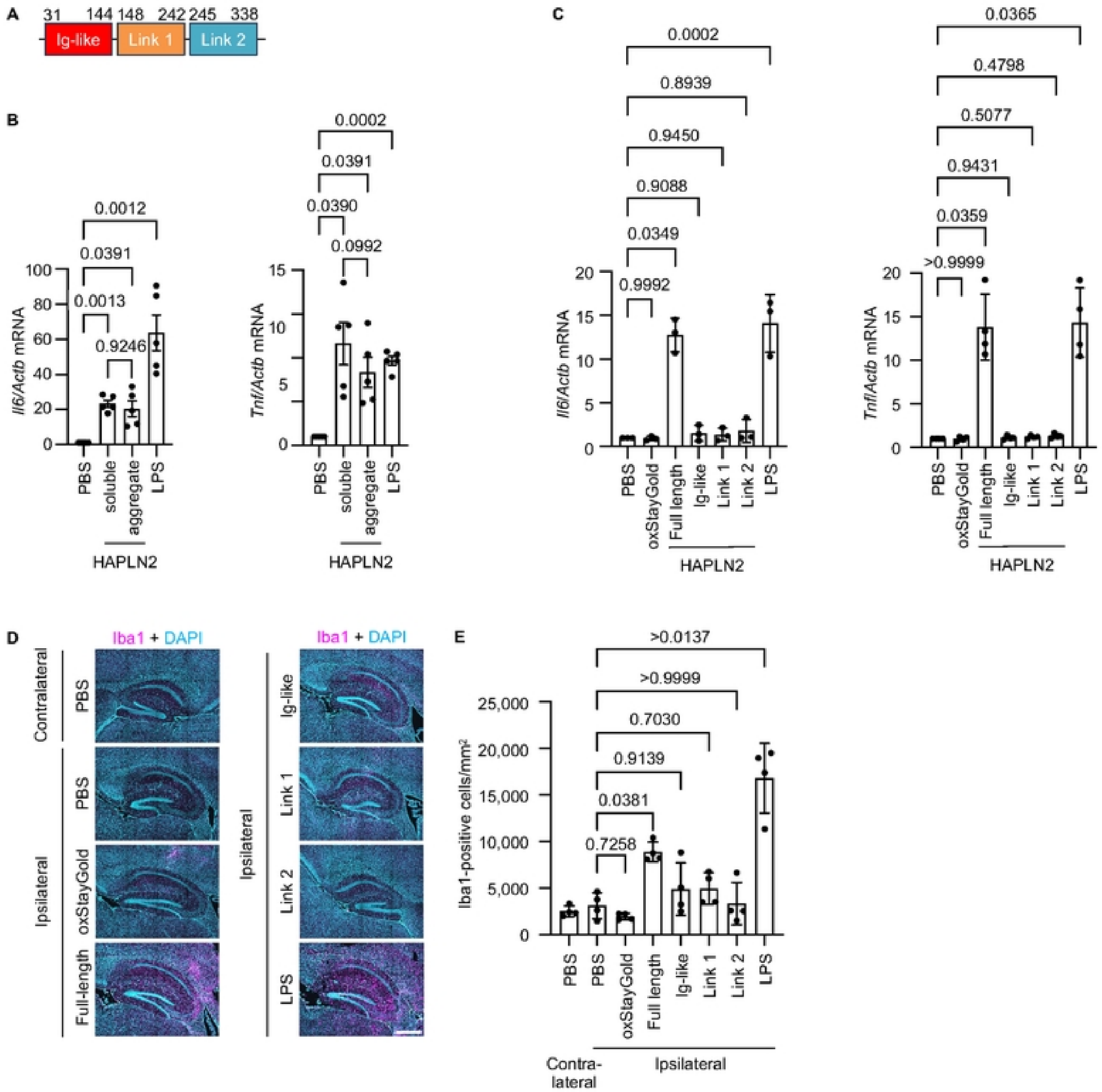
A
31
144
148
242
245
338
Ig-like
Link 1
Link 2
B
Il6/Actb mRNA
0.0012
0.0391
0.0013
0.9246
PBS
soluble
aggregate
LPS
HAPLN2
Tnf/Actb mRNA
0.0002
0.0391
0.0390
0.0992
C
0.0002
0.8939
0.9450
0.9088
0.0349
0.9992
0.0365
0.4798
0.5077
0.9431
0.0359
>0.9999
oxStayGold
Full length
Ig-like
Link 1
Link 2
D
Iba1 + DAPI
Contralateral
Ipsilateral
PBS
oxStayGold
Full-length
Ig-like
Link 1
Link 2
LPS
E
Iba1-positive cells/mm²
>0.0137
>0.9999
0.7030
0.9139
0.0381
0.7258
Contra-
lateral
Ipsilateral

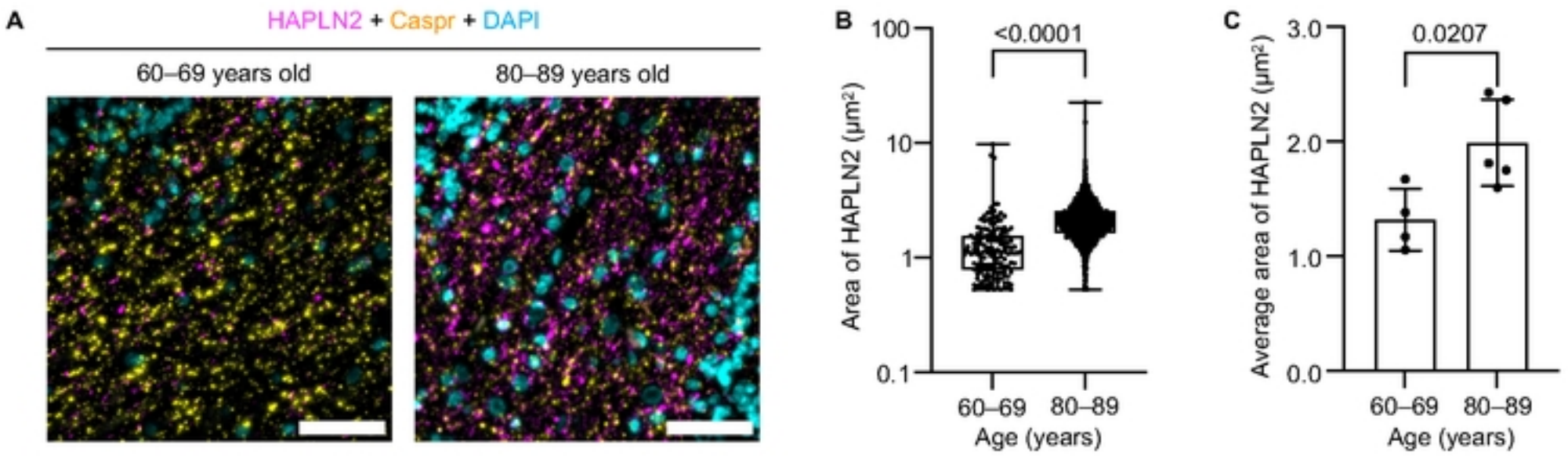
A
HAPLN2 + Caspr + DAPI
60–69 years old
80–89 years old
B
<0.0001
Area of HAPLN2 (μm²)
100
10
1
0.1
60–69
80–89
Age (years)
C
0.0207
Average area of HAPLN2 (μm²)
3.0
2.0
1.0
0.0
60–69
80–89
Age (years)